ABSTRACT

Title of Dissertation: Electro-optic Microwave Receivers at the System and Device Level

Steven Thomas Lipkowitz
Doctor of Philosophy, 2023

Dissertation Directed by: Dr. Thomas E. Murphy
Department of Electrical and Computer Engineering

Photonic microwave receivers take advantage of optical components and techniques to detect, transmit, and process microwave signals. These systems are able to take advantage of low-loss fiber-optic transmission in situations where coaxial cables would be prohibitively lossy, and are able to make use of integrated optical components that are much smaller and lighter than their microwave counterparts. Additionally, optical techniques can enable signal processing operations that are either difficult or impossible to perform using electrical methods. For these systems to work, an electrical-to-optical converter must be implemented to convert incoming microwave signals to the optical domain. A common method for this electrical-to-optical conversion is to make use of an electro-optic material, wherein the optical refractive index is modulated by the microwave electric field. These electro-optic modulators are commercially available in a variety of configurations with microwave bandwidths in the tens of gigahertz. Once the microwave signal is converted, other commercial optical components (filters, splitters, etc.) can be introduced to further process the signal, which is ultimately converted back to the electrical domain via

photo-detection. At the system level, novel techniques for combining commercial components to perform advanced signal processing are rapidly emerging. At the device level, new chip-scale techniques for performing electro-optic modulation are also being developed. Some of these techniques involve using well known electro-optic materials in new ways, while others involve exploring lesser known materials and investigating their performance.

In this thesis I will discuss experiments at both the system and device level. At the system level, I implemented a photonic down-converting I/Q mixer using commercial microwave and optical components. The system uses an electro-optic modulator that simultaneously converts both a microwave signal and local oscillator (LO) to the optical regime, where careful filtering and photo-detection of the optical signal produces two output electrical signals at an intermediate frequency that is the difference between the original LO and microwave frequencies. These two outputs are identical, except that they differ in phase by 90 degrees. This lower frequency output allows for easier digitization of the electrical signal, and the phase diversity of the outputs allows for further signal processing to be performed in the electrical domain.

At the device level, I designed, fabricated, and characterized an on-chip metal-free doubly-resonant electro-optic modulator using aluminum nitride (AlN) as the electro-optic material. Aluminum nitride is a wide band gap material with a significant electro-optic response, allowing for low-loss optical transmission over a large bandwidth. Additionally, AlN is significantly easier to work with than other electro-optic materials such as the popular lithium niobate. The doubly resonant device design discussed here takes advantage of the electric field buildup that occurs in resonant structures. In the microwave regime, a high-epsilon dielectric resonator antenna (DRA) is used to enhance the field strength of incoming microwave radiation as well as change the direction of the incident field. This DRA is placed atop an optical resonator fabricated in AlN on-chip,

where the enhanced microwave near field of the DRA is allowed to interact with the built up optical field in the AlN resonator. This double resonance allows for a significant enhancement in the strength of the conversion from electrical to optical. This device also boasts an entirely metal-free composition, which allows for greater immunity against electromagnetic attack than conventional antenna structures.

Electro-optic Microwave Receivers at the System and Device Level

by

Steven Thomas Lipkowitz

Dissertation submitted to the Faculty of the Graduate School of the
University of Maryland, College Park in partial fulfillment
of the requirements for the degree of
Doctor of Philosophy
2023

Advisory Committee:
Dr. Thomas E. Murphy, Chair/Advisor
Dr. Karen E. Grutter
Dr. Yanne K. Chembo
Dr. Thomas M. Antonsen, Jr.
Dr. Steven M. Anlage (Dean's Representative)

Acknowledgments

There are many people who have helped me achieve this milestone, and while I cannot thank them all individually, there are a few I would like to acknowledge. I would like to thank my parents for everything they've done throughout my life to help me get here. I would like to thank my wife for standing by me during the difficult times and for celebrating alongside me during times of success. I would like to thank my advisor, Tom, for being a fantastic mentor who was always eager to help however he could. I would like to thank all the colleagues and peers who supported and encouraged me. Finally, I would like to thank all the friends and family that have been by my side throughout this journey.

Table of Contents

List of Tables

List of Figures

List of Abbreviations

AlN	Aluminum nitride
AMZI	Asymmetric Mach-Zehnder interferometer
DDMZM	Dual drive Mach-Zehnder modulator
DRA	Dielectric resonant antenna
EMI	Electromagnetic interference
FEM	Finite element method
FSR	Free spectral range
FWHM	Full width at half max
ICPRIE	Inductively coupled plasma reactive ion etch
IMD3	Third order intermodulation distortion
LO	Local oscillator
$LiNbO_3$	Lithium niobate
MOCVD	Metal-organic chemical vapor deposition
MZM	Mach-Zehnder modulator
MWP	Microwave photonic
OBPF	Optical band pass filter
OSA	Optical spectrum analyzer
PECVD	Plasma enhanced chemical vapor deposition
PM	Polarization maintaining
Si	Silicon
SiO_2	Silicon dioxide
SFDR	Spurious free dynamic range

Chapter 1: Introduction

1.1 Overview of microwave photonics

Microwave photonic (MWP) systems operate by converting microwave frequency electrical signals to the optical domain. Once converted, these signals can then take advantage of low-loss fiber optic transmission, as well as optical techniques for signal processing that may be either difficult or impossible to duplicate electrically. The advantage of fiber optic transmission becomes especially apparent over distances where the weight and loss characteristics of optical fiber greatly outperform standard coaxial cables [2]. Additionally, optical fibers have a much larger bandwidth than coaxial cables, allowing for multiple frequency multiplexed signals to be transmitted simultaneously. MWP systems are also inherently more immune to electromagnetic interference than electrical microwave systems.

Electro-optic modulation is a popular way of converting microwave signals to the optical domain and Figure 1.1 shows a schematic of a typical MWP link using this method. Electro-optic modulators are made from a material with a significant second order-nonlinear susceptibility. Within these materials, the refractive index of a traveling optical wave is modified by the electric field of a microwave signal. Lithium niobate ($LiNbO_3$) is a popular choice of electro-optic material, as it has a strong second order response, and allows for low loss optical transmission at wavelengths used for telecommunications. Most commercially available $LiNbO_3$ modulators

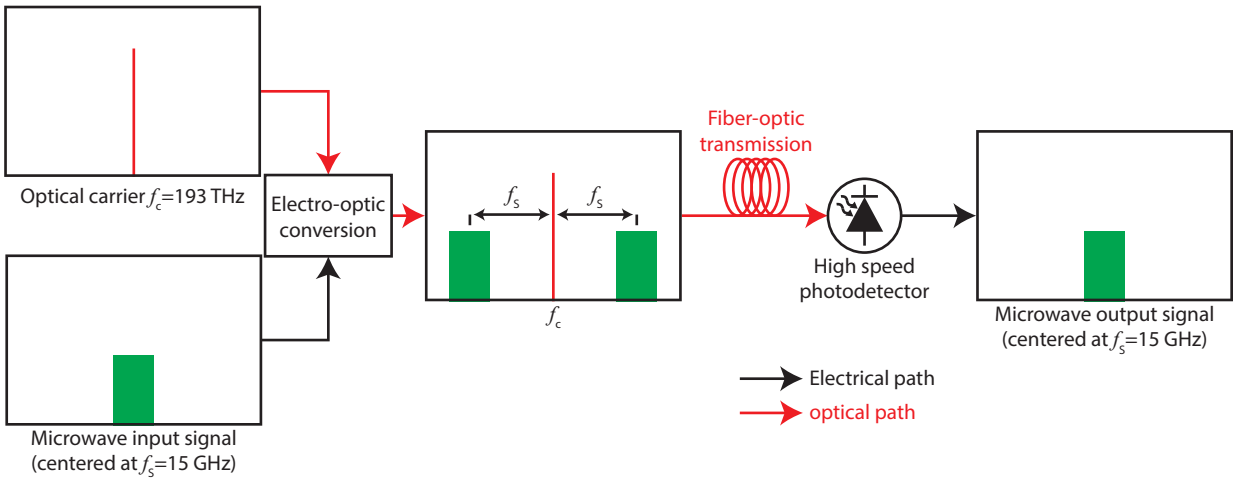

Figure 1.1: Schematic of a typical MWP link using electro-optics to convert from microwave to optical. Microwave and optical waves are combined in an electro-optic device to produce the converted microwave signal, which is then free to propagate along optical fiber before being converted back to a microwave signal via photodetection.

make use of titanium diffusion or annealed proton exchange to form optical waveguides within bulk $LiNbO_3$ substrates [3]. These processes are in general not CMOS compatible, and produce waveguides that are very weakly guiding and thus require the electrodes carrying the microwave signal to be placed far from the optical waveguides to prevent conductive loss [4]. This results in weaker microwave electric fields in the lithium niobate waveguides, necessitating that the interaction length be on the order of a centimeter or more. Recently, chip-scale thin film $LiNbO_3$ modulators have been reported with operating frequencies up to 110 GHz [5, 6]. However these devices require either crystal ion slicing [7, 8] or precise backside polishing [9] each of which are challenging. Additionally, dry etching of $LiNbO_3$ can be difficult [10], and often involves ion milling [11]. Sputtered aluminum nitride (AlN) provides a promising alternative to lithium niobate due to less challenging preparation and patterning techniques [12], and will be discussed in depth in chapter 3.

1.2 The electro-optic effect

In an electo-optic material, the refractive index of light propagating through the material is modified by an external electric field. To understand this phenomenon, we begin with the displacement field $\mathbf{D}$

$$\mathbf{D} = \epsilon_0 \mathbf{E} + \mathbf{P} \tag{1.1}$$

where $\mathbf{E}$ is the vector electric field and $\mathbf{P}$ is the material polarization. In the simplest case, $\mathbf{P}$ is directly proportional to the electric field and we have that $\mathbf{P} = \epsilon_0 \chi \mathbf{E}$ where the susceptibility χ is a scalar constant. In the more general anisotropic (but still linear) case $\mathbf{P} = \epsilon_0 \chi^{(1)} \mathbf{E}$, where $\chi^{(1)}$ is a second rank tensor. Here the superscript (1) is used to denote that the susceptibility is first order (linear), and is not used to denote exponentiation. In the linear case, the relationship between polarization and electric field can be easily represented with matrices as shown below:

$$\begin{bmatrix} P_1 \\ P_2 \\ P_3 \end{bmatrix} = \epsilon_0 \begin{bmatrix} \chi_{11}^{(1)} & \chi_{12}^{(1)} & \chi_{13}^{(1)} \\ \chi_{21}^{(1)} & \chi_{22}^{(1)} & \chi_{23}^{(1)} \\ \chi_{31}^{(1)} & \chi_{32}^{(1)} & \chi_{33}^{(1)} \end{bmatrix} \begin{bmatrix} E_1 \\ E_2 \\ E_3 \end{bmatrix} \tag{1.2}$$

where subscripts 1, 2, and 3 refer to three orthogonal unit vectors. In general, the susceptibility need not be linear. In this case we have the following equation for polarization:

$$\mathbf{P} = \epsilon_0 (\chi^{(1)} \mathbf{E} + \chi^{(2)} \mathbf{E}\mathbf{E} + \chi^{(3)} \mathbf{E}\mathbf{E}\mathbf{E} + \ldots) \tag{1.3}$$

where $\chi^{(n)}$ represents the n^{th} order susceptibility and is a tensor of rank $n+1$. The contribution to the polarization from the higher order susceptibility tensors cannot easily be represented with matrices. As a result we will adopt the following notation for $\mathbf{P}$:

$$P_i = \epsilon_0(\chi_{ik}E_k + \chi_{ikl}E_kE_l + \chi_{iklm}E_kE_lE_m + \ldots) \tag{1.4}$$

where i, k, l, and m each take on values of 1, 2, or 3, and Einstein summation convention is used. The superscript labels are now unnecessary as well, as $\chi^{(n)}$ must have exactly $n+1$ subscripts. The electro-optic effect arises from the second order susceptibility, so we will consider only first and second order contributions to the polarization from now on.

We will now consider the case where E consists of a monochromatic plane wave, and an external DC electric field. We then have

$$\mathbf{E}(\mathbf{r},t) = \left[\frac{1}{2}\mathbf{A}(\mathbf{r},\omega)e^{j(\omega t-\kappa\cdot\mathbf{r})} + C.C.\right] + \mathbf{E}(0) \tag{1.5}$$

$$\mathbf{P}(\mathbf{r},t) = \left[\frac{1}{2}\mathbf{P}(\mathbf{r},\omega)e^{j(\omega t-\kappa\cdot\mathbf{r})} + C.C.\right] + \mathbf{P}(0) \tag{1.6}$$

where $C.C.$ denotes the complex conjugate, $\mathbf{r}$ reperesents the location in space, and κ is the wave vector at frequency ω. By choosing this form for the electric field and polarization, we have chosen to restrict our focus to the field oscillating at frequency ω and neglect other frequency terms. In general the n^{th} order susceptibility is a function of the n frequencies of its associated

electric fields:

$$\chi_{ik} \rightarrow \chi_{ik}(-\omega, \omega) \tag{1.7}$$

$$\chi_{ikl} \rightarrow \chi_{ikl}(-\omega_3; \omega_1, \omega_2) \tag{1.8}$$

where the argument prior to the semicolon is the negative of the oscillation frequency of the resulting term and is chosen such that the sum of all $n+1$ arguments is 0 (e.g. the $\chi_{ikl}(-\omega_3; \omega_1, \omega_2)$ term oscillates at frequency $\omega_3 = \omega_1 + \omega_2$). It is important to note that in general the nonlinear susceptibility tensors are not uniquely defined. In order to avoid ambiguity in their definitions, we enforce intrinsic permutation symmetry. That is we enforce that $\chi_{ikl}(-\omega_3; \omega_1, \omega_2) = \chi_{ilk}(-\omega_3; \omega_2, \omega_1)$. This leads to a degeneracy factor $K(-\omega_3; \omega_1, \omega_2)$ in the polarization:

$$K(-\omega_3; \omega_1, \omega_2) = P(2^{(l+m-2)}) \tag{1.9}$$

$P =$ # of distinct permutations of ω_1, ω_2

$m =$ # of input frequencies that are 0

$$l = \begin{cases} 0 \text{ if } \omega_3 = 0 \\ 1 \text{ otherwise} \end{cases}$$

We then have

$$P_i(\mathbf{r}, \omega) = \epsilon_0 \left[\chi_{ik}(-\omega; \omega) A_k(\mathbf{r}, \omega) + 2\chi_{ikl}(-\omega; \omega, 0) A_k(\mathbf{r}, \omega) E_l(0)\right] \tag{1.10}$$

$$D_i(\mathbf{r}, \omega) = \epsilon_0 \left[A_i(\mathbf{r}, \omega) + \chi_{ik}(-\omega; \omega) A_k(\mathbf{r}, \omega) + 2\chi_{ikl}(-\omega; \omega, 0) A_k(\mathbf{r}, \omega) E_l(0)\right] \tag{1.11}$$

We can factor $A_k(\mathbf{r},\omega)$ out of equation 1.11 yielding

$$D_i(\mathbf{r},\omega) = \epsilon_0 \left[\delta_{ik} + \chi_{ik}(-\omega;\omega) + 2\chi_{ikl}(-\omega;\omega,0)E_l(0)\right] A_k(\mathbf{r},\omega) \tag{1.12}$$

where $\delta_{ik} = 1$ if $i = k$ and 0 otherwise. Here $\epsilon_0(\delta_{ik} + \chi_{ik}(-\omega;\omega))$ is the familiar linear permittivity tensor $\epsilon^{(1)}$ of the material. The term $2\epsilon_0\chi_{ikl}(-\omega;\omega,0)E_l(0) = \delta\epsilon$ can then be viewed as the electro-optic change in the permittivity tensor: $\epsilon = \epsilon^{(1)} + \delta\epsilon$. Since in general the electric field need not be perpendicular to the propagation direction κ, it is convenient to convert from $\mathbf{E}$ to $\mathbf{D}$ using $\mathbf{E} = \epsilon^{-1}\mathbf{D}$ as $\mathbf{D}$ must perpendicular to both κ and magnetic field $\mathbf{B}$ according to Maxwell's equations. We then define

$$\eta = (\eta^{(1)} + \delta\eta) = \epsilon_0\epsilon^{-1} \tag{1.13}$$

$$\delta\eta_{ik} = r_{ikl}E_l(0) \tag{1.14}$$

where $\eta^{(1)} = \epsilon_0(\epsilon^{(1)})^{-1}$ and the tensor r is known as the electro-optic tensor. Using that $(\eta^{(1)} + \delta\eta)\left[(\eta^{(1)})^{-1} + \frac{\delta\epsilon}{\epsilon_0}\right] = I$ where I is the identity matrix, we have

$$\eta^{(1)}\frac{\delta\epsilon}{\epsilon_0} + \delta\eta\left[\eta^{(1)}\right]^{-1} = 0 \tag{1.15}$$

where we have neglected the term on the order of δ^2 under the assumption that the electro-optic change is small compared to the linear case. Solving for $\delta\eta$ we have

$$\delta\eta = -\eta^{(1)}\frac{\delta\epsilon}{\epsilon_0}\eta^{(1)} \tag{1.16}$$

by appropriate choice of coordinates, we can ensure that $\eta^{(1)}$ is diagonal with $\eta^{(1)}_{ik} = \frac{\delta_{ik}}{n_i^2}$ where $n_i^2 = \frac{\epsilon_{ii}}{\epsilon_0}$. Therefore

$$\begin{aligned}\delta\eta_{ik} &= -\frac{\delta_{il}}{n_i^2}\frac{\delta\epsilon_{lm}}{\epsilon_0}\frac{\delta_{mk}}{n_m^2} \\ &= -\frac{2\chi_{ikl}(-\omega;\omega,0)E_l(0)}{n_i^2 n_k^2}\end{aligned} \tag{1.17}$$

and

$$r_{ikl} = -\frac{2\chi_{ikl}(-\omega;\omega,0)}{n_i^2 n_k^2} \tag{1.18}$$

If the material in question is lossless, it follows that η must be real and symmetric. Thus $\delta\eta_{ik} = \delta\eta_{ki}$ and $r_{ikl} = r_{kil}$. This allows us to contract the indices i and k into one index m ranging from 1 to 6. The relationship between the indices is as follows:

$$ik = \begin{bmatrix} 11 & 12 & 13 \\ 21 & 22 & 23 \\ 31 & 32 & 33 \end{bmatrix} \leftrightarrow \begin{bmatrix} 1 & 6 & 5 \\ 6 & 2 & 4 \\ 5 & 4 & 3 \end{bmatrix} = m \tag{1.19}$$

1.2.1 Crystallographic symmetry

In principle, the second order susceptibility has 27 elements: three for each of its indices. In reality however, the form of the susceptibility is restricted by the symmetry of the material in question. This means that if the material appears identical after unitary transformation R, the susceptibility must also be identical after transformation by R. Here R can be represented by a

3x3 matrix, and applying R to the susceptibility is done by applying the rotation identically for each index of χ:

$$\chi'_{ik} = R_{il}R_{km}\chi_{lm} \tag{1.20}$$

$$\chi'_{ikl} = R_{im}R_{kn}R_{lo}\chi_{mno} \tag{1.21}$$

One important consequence of this is that, for any centrosymmetric material, the second order susceptibility must be 0. This is because for a centrosymmetric transformation

$$R = \begin{bmatrix} -1 & 0 & 0 \\ 0 & -1 & 0 \\ 0 & 0 & -1 \end{bmatrix} \tag{1.22}$$

$$R_{ik} = -\delta_{ik} \tag{1.23}$$

and therefore $\chi'_{ikl} = -\chi_{ikl} = \chi_{ikl}$, meaning $\chi_{ikl} = 0$. Among the remaining non-centrosymmetric crystal groups, other symmetries may reduce the number of unique terms. Table 1.1 shows the form of the contracted electro-optic tensor r for the allowed crystal symmetry groups. It is worth noting that while this analysis is valid for the material bulk, crystal symmetries can be broken by material interfaces and the electro-optic effect has been reported at the interface of otherwise amorphous material [13].

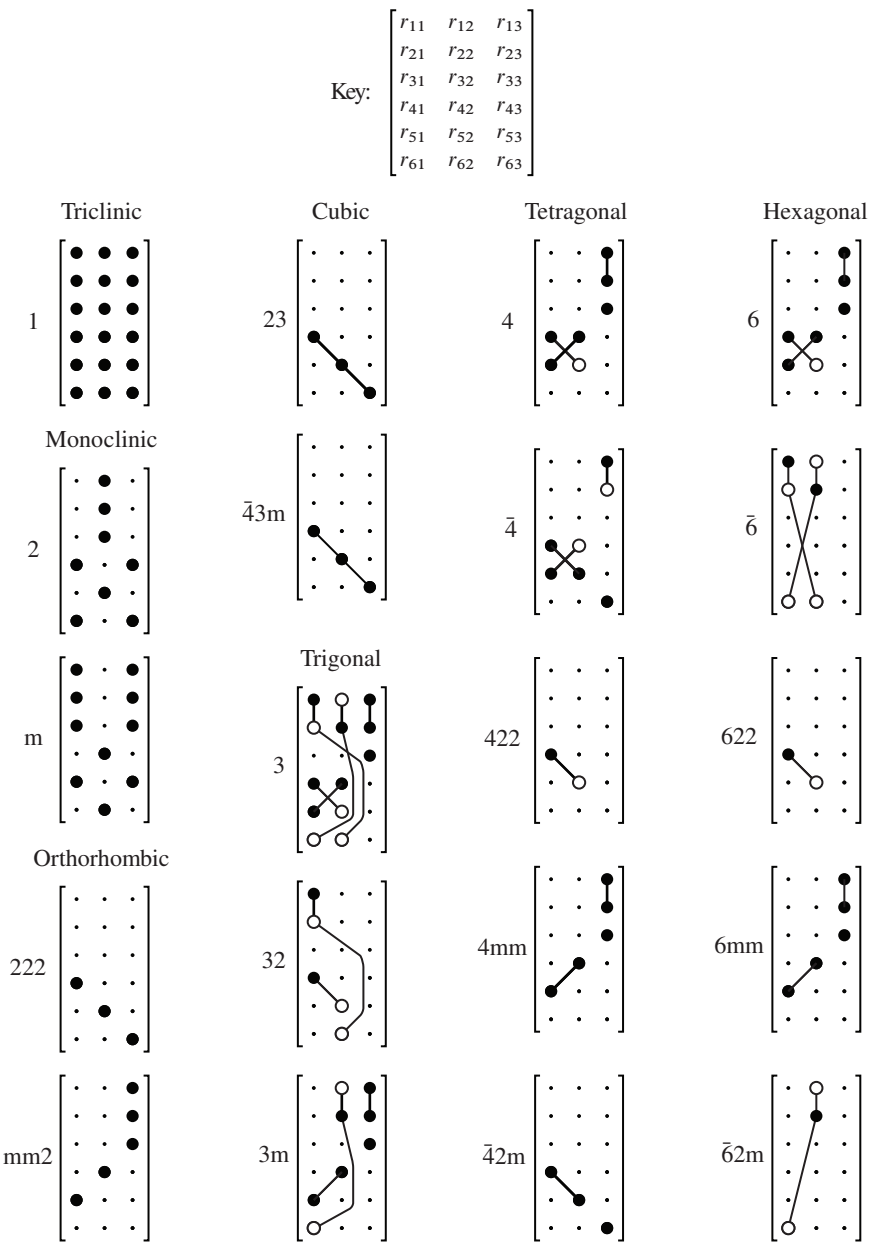

Table 1.1: Form of the electro-optic tensor for the allowed symmetry groups. Connected filled symbols are equal, while connected filled and unfilled symbols are equal and opposite. Reused with permission from Thomas E. Murphy's lecture notes, unpublished

1.2.2 Phase modulation

Using the electro-optic effect, we are able to modify the phase shift experienced by a wave as it propagates through a given length L of electro-optic material. Let us choose the following labels for our basis vectors:

$$(x, y, z) \leftrightarrow (1, 2, 3) \tag{1.24}$$

For simplicity, we begin with a plane wave linearly polarized in the y direction, and propagating in the x direction. We will further assume that we have chosen x, y and z such that η is diagonal. Finally, we include an external DC electric field E_0 in the z direction. We then have

$$\mathbf{E}(x, t) = \hat{y} E_y e^{j(\omega_0 t - \kappa_0 x)} \tag{1.25}$$

$$\kappa_0 = \frac{2\pi n_y(\omega)}{\lambda_0} \tag{1.26}$$

where $\omega_0 = 2\pi f_0$, f_0 is the frequency of oscillation, λ_0 is the wavelength, and $n_y(\omega_0) = \sqrt{\epsilon_y(\omega_0)/\epsilon_0}$ is the material refractive index for the y-polarized wave. Here since the input optical field is monochromatic, we have adopted phasor notation. We may then write $n_y(\omega_0)$ in terms of η_y using equation 1.13:

$$n_y(\omega_0) = \left[\eta_y^{(1)}(\omega_0) + \delta\eta_y(\omega_0)\right]^{-\frac{1}{2}} \tag{1.27}$$

where $\eta_y^{(1)}(\omega_0)$ represents η in the absence of an external DC field and $\eta_y^{(1)}(\omega_0) = \frac{1}{(n_y^{(1)})^2}$. In most cases, $\delta\eta \ll \eta_0$ and we may simplify the exponent using Taylor expansion. This yields

$$n_y(\omega_0) = n_y^{(1)} \left[1 - \frac{1}{2}\frac{\delta\eta_y(\omega_0)}{\eta_y^{(1)}(\omega_0)}\right] \tag{1.28}$$

$$= n_y^{(1)} - \frac{1}{2}(n_y^{(1)})^3 r_{23} E_0 \tag{1.29}$$

$$= n_y^{(1)} + \delta n_y \tag{1.30}$$

The phase shift θ accumulated by E_y as it passes from $x = 0$ to $x = L$ is then

$$\theta = \frac{2\pi n_y^{(1)} L}{\lambda_0} + \frac{2\pi\delta n_y L}{\lambda_0} = \theta_0 + \delta\theta \tag{1.31}$$

$$\theta_0 \equiv \frac{2\pi n_y^{(1)} L}{\lambda_0} \tag{1.32}$$

$$\delta\theta \equiv \frac{2\pi\delta n_y L}{\lambda_0} \tag{1.33}$$

This allows us to control the output phase by controlling the DC electric field.

Now suppose that the external electric field is not DC, but instead oscillates at some microwave frequency $\Omega \ll \omega_0$:

$$E_0 = A_0 \sin(\Omega t + \phi) \tag{1.34}$$

where ϕ is some phase offset. Provided $L \ll \lambda_\Omega$ where λ_Ω is the microwave wavelength, it is

sufficient to add a simple sinusoidal dependence to $\delta\theta$:

$$\theta = \theta_0 - \delta\theta_\Omega \sin(\Omega t + \phi) \tag{1.35}$$

$$\delta\theta_\Omega = \frac{\pi L}{\lambda_0}(n_y^{(1)})^3 r_{23} A_0 \tag{1.36}$$

We then have that after traveling distance L

$$\mathbf{E}(L,t) = \hat{y} E_y e^{j(\omega_0 t)} e^{-j\theta_0} e^{j\delta\theta_\Omega \sin(\Omega t+\phi)} \tag{1.37}$$

By applying the well known Jacobi-Anger expansion, we can decompose this time varying phase into a series of frequency components:

$$e^{j\delta\theta_\Omega \sin(\Omega t+\phi)} = \sum_{n=-\infty}^{\infty} J_n(\delta\theta_\Omega) e^{jn(\Omega t+\phi)} \tag{1.38}$$

Where J_n is the n^{th} order Bessel function of the first kind. Since we have assumed $\delta\theta_\Omega \ll 1$, we can expand these Bessel functions to first order in $\delta\theta_\Omega$, yielding

$$e^{j\delta\theta_\Omega \sin(\Omega t+\phi)} = 1 + \frac{\delta\theta_\Omega}{2}(e^{j(\Omega t+\phi)} - e^{-j(\Omega t+\phi)}) \tag{1.39}$$

By plugging equation 1.39 into equation 1.37 we can see that $\mathbf{E}(L,t)$ consists of three distinct

frequency components:

$$\omega_0 \tag{1.40}$$

$$\omega_+ = \omega_0 + \Omega \tag{1.41}$$

$$\omega_- = \omega_0 - \Omega \tag{1.42}$$

The newfound components at ω_+ and ω_- are referred to as modulation sidebands, and their amplitudes are directly proportional to the microwave electric field, provided the field strength remains weak so as to not violate our assumption that $\delta\theta_\Omega \ll 1$.

1.2.3 Intensity modulation

Although modulating the phase of light with an external microwave frequency field produces modulation sidebands on the optical signal, a standard photodetector will not detect modulation of the phase alone. This is because, for a standard photodetector, the photocurrent is proportional to the optical power incident on the detector.

$$I(t) = R|E(t)|^2 \tag{1.43}$$

where $I(t)$ is the output photocurrent, $|E(t)|^2$ is the optical power incident on the detector, and R is the detector responsivity. Plugging equation 1.37 into equation 1.43 we see that

$$I(t) = R|\mathbf{E}(L,t)|^2 = R|E_y|^2 \tag{1.44}$$

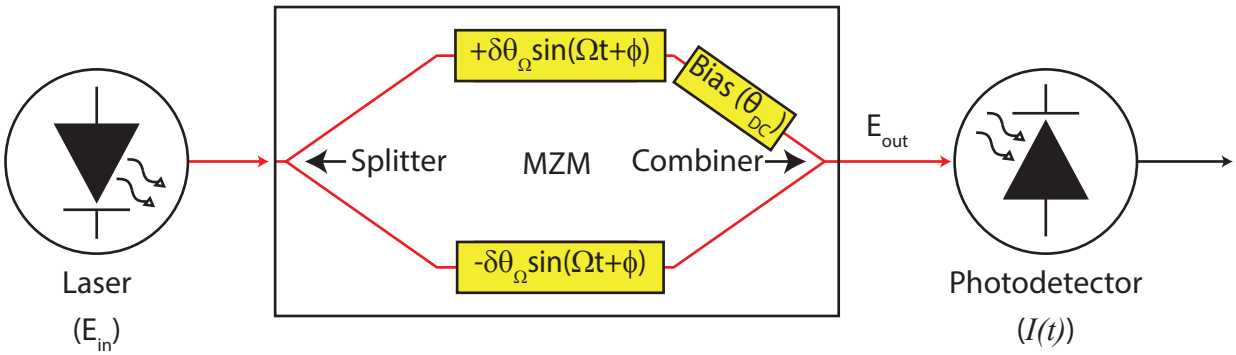

Figure 1.2: Schematic diagram of an MZM device.

and photodection of a phase modulated signal yields a DC photocurrent, just as though the field had not been modulated at all. If one wants to detect a signal at frequency Ω one needs to convert the phase modulation to intensity modulation. One common way of converting phase modulation of an optical field to intensity modulation is via a Mach-Zehnder modulator (MZM). Figure 1.2 shows a schematic of an MZM device, which splits the optical path into two arms, applies an equal but opposite microwave electric field to each arm, then recombines the optical fields. A separate DC electric field applied to only one arm is used to control the relative phase of the two arms. Mathematically we can represent each step of this process via matrices:

$$E_{out} = \underbrace{\left(\frac{1}{\sqrt{2}}\begin{bmatrix}1 & j\end{bmatrix}\right)}_{\text{combiner}} \underbrace{\left(\begin{bmatrix} e^{j(\delta\theta_\Omega \sin(\Omega t+\phi)+\theta_{\text{DC}})} & 0 \\ 0 & e^{-j\delta\theta_\Omega \sin(\Omega t+\phi)}\end{bmatrix}\right)}_{\text{phase shifts}} \underbrace{\left(\frac{1}{\sqrt{2}}\begin{bmatrix}1 \\ j\end{bmatrix}\right)}_{\text{splitter}} E_{in} \quad (1.45)$$

where θ_{DC} represents the relative phase of the two arms controlled by the DC field. Then

$$E_{out} = \frac{E_{in}}{2}\left\{e^{j\theta_{\text{DC}}}\left[1+\frac{\delta\theta_\Omega}{2}(e^{j(\Omega t+\phi)}-e^{-j(\Omega t+\phi)})\right]-\left[1-\frac{\delta\theta_\Omega}{2}(e^{j(\Omega t+\phi)}+e^{-j(\Omega t+\phi)})\right]\right\} \tag{1.46}$$

$$= E_{in}e^{\frac{j\theta_{\text{DC}}}{2}}\left\{j\sin\left(\frac{\theta_{\text{DC}}}{2}\right)+\frac{\delta\theta_\Omega}{2}\cos\left(\frac{\theta_{\text{DC}}}{2}\right)\left[e^{j(\Omega t+\phi)}-e^{-j(\Omega t+\phi)}\right]\right\} \tag{1.47}$$

and the photocurrent

$$I(t) = R|E_{out}|^2 = R|E_{in}|^2\left\{\sin^2\left(\frac{\theta}{2}\right)+\delta\theta_\Omega\sin(\theta)\sin(\Omega t+\phi)\right\} \tag{1.48}$$

Here we can see that for the right choice of θ_{DC}, we do obtain a photocurrent oscillating at frequency Ω. To maximize this photocurrent, we should apply a DC electric field such that $\theta_{\text{DC}} = \frac{\pi}{2}$. This is known as biasing the modulator at quadrature.

1.2.4 Nonlinear wave equation

In the case that the microwave wavelength and the interaction length L are comparable, it is no longer sufficient to describe $\delta\theta_\Omega$ as in equation 1.36. In this case, we must from the beginning consider an electric field consisting of three frequency components along with the microwave electric field

$$\begin{aligned}\mathbf{E}(x,t) = &\frac{1}{2}\left[A_0(x,\omega_0)e^{j(\omega_0 t-\kappa_0 x)}+A_+(x,\omega_+)e^{j(\omega_+ t-\kappa_+ x)}+A_-(x,\omega_-)e^{j(\omega_- t-\kappa_- x)}+C.C.\right]\hat{y}\\ &+\frac{1}{2}\left[-jA_\Omega(x,\Omega)e^{j\Omega t}+C.C.\right]\hat{z}\end{aligned} \tag{1.49}$$

where $\omega_{(0,+,-)}$ are defined in equations 1.40-1.42, and $\kappa_{(0,+,-)} = \frac{2\pi n}{\lambda_{(0,+,-)}} = \frac{n\omega_{(0,+,-)}}{c}$ where $\lambda_{(0,+,-)}$ is the optical wavelength and $c = \frac{1}{\sqrt{\mu_0 \epsilon_0}}$ is the speed of light in vacuum. Here we have again abandoned phasor notation and for simplicity we will assume that the material in question is non-magnetic ($\mu = \mu_0$) and the refractive index n is constant over the frequency range of interest. Then from Maxwell's equations, we have

$$\nabla \times \nabla \times \mathbf{E} = \mu_0 \frac{\partial^2 \mathbf{D}}{\partial t^2} \tag{1.50}$$

$$\mathbf{D} = \epsilon \mathbf{E} + \mathbf{P}^{(2)} \tag{1.51}$$

where ϵ includes contributions from the linear susceptibility. Separating terms by frequency and assuming that the $A(x)$ are slowly varying such that $\frac{\partial^2 A(x)}{\partial x^2} \ll \kappa \frac{\partial A(x)}{\partial x}$, equation 1.50 yields the following coupled differential equations:

$$\begin{aligned} \frac{\partial A_0(x,\omega_0)}{\partial x} = \frac{\omega_0}{2nc} \big[& \chi_{yyz}(-\omega_0, \omega_+, -\Omega) A_+(x,\omega_+) A_\Omega^*(x,\Omega) e^{-j(\kappa_+ - \kappa_0)x} \\ & - \chi_{yyz}(-\omega_0, \omega_-, \Omega) A_-(x,\omega_-) A_\Omega(x,\Omega) e^{-j(\kappa_- - \kappa_0)x} \big] \end{aligned} \tag{1.52}$$

$$\frac{\partial A_+(x,\omega_+)}{\partial x} = -\frac{\omega_+}{2nc} \chi_{yyz}(-\omega_+, \omega_0, \Omega) A_0(x,\omega_0) A_\Omega(x,\Omega) e^{-j(\kappa_0 - \kappa_+)x} \tag{1.53}$$

$$\frac{\partial A_-(x,\omega_-)}{\partial x} = \frac{\omega_-}{2nc} \chi_{yyz}(-\omega_-, \omega_0, -\Omega) A_0(x,\omega_0) A_\Omega^*(x,\Omega) e^{-j(\kappa_0 - \kappa_-)x} \tag{1.54}$$

Provided the modulation is weak, we can assume $\frac{\partial A_0(x,\omega_0)}{\partial x} \approx 0$ as $A_{(+,-)} \ll A_0$. Additionally, for $\Omega \ll \omega_0$, we can assume $\omega_+ \approx \omega_- \approx \omega_0$ and $\chi_{yyz}(-\omega_+, \omega_0, \Omega) \approx \chi_{yyz}(-\omega_-, \omega_0, -\Omega) \approx$

$\chi_{yyz}(-\omega_0, \omega_0, 0)$. Then

$$\frac{\partial A_0(x,\omega_0)}{\partial x} = 0 \tag{1.55}$$

$$\frac{\partial A_+(x,\omega_+)}{\partial x} = \frac{\omega_0 n^3}{4c} r_{23} A_0(0,\omega_0) A_\Omega(x,\Omega) e^{j\Delta\kappa x} \tag{1.56}$$

$$\frac{\partial A_-(x,\omega_-)}{\partial x} = -\frac{\omega_0 n^3}{4c} r_{23} A_0(0,\omega_0) A^*_\Omega(x,\Omega) e^{-j\Delta\kappa x} \tag{1.57}$$

Where $\Delta\kappa = \kappa_0 - \kappa_- = -(\kappa_0 - \kappa_+) = \frac{2\pi n}{\lambda_\Omega}$. Assuming $A_+(0,\omega_+) = A_-(0,\omega_-) = 0$, we can integrate to find solutions after propagation length L in terms of $A_0(0,\omega_0)$ and $A_\Omega(0,\Omega)$

$$A_+(L,\omega_+) = \frac{\omega_0 n^3}{4c} r_{23} A_0(0,\omega_0) \int_0^L A_\Omega(x,\Omega) e^{j\Delta\kappa x} dx \tag{1.58}$$

$$A_-(x,\omega_-) = -\frac{\omega_0 n^3}{4c} r_{23} A_0(0,\omega_0) \int_0^L A^*_\Omega(x,\Omega) e^{-j\Delta\kappa x} dx \tag{1.59}$$

If we further assume that $A(x,\Omega)$ is uniform in x, this yields

$$A_+(L,\omega_+) = 2\frac{\omega_0 n^3}{\Delta\kappa 4c} r_{23} A_0(0,\omega_0) A_\Omega(0,\Omega) e^{\frac{j\Delta\kappa L}{2}} \sin\left(\frac{\Delta\kappa L}{2}\right) \tag{1.60}$$

$$A_-(L,\omega_-) = -2\frac{\omega_0 n^3}{\Delta\kappa 4c} r_{23} A_0(0,\omega_0) A^*_\Omega(0,\Omega) e^{-\frac{j\Delta\kappa L}{2}} \sin\left(\frac{\Delta\kappa L}{2}\right) \tag{1.61}$$

Here we see that the amplitudes of the sidebands at $\omega_{(+,-)}$ do not depend linearly on L when L and λ_Ω are comparable. In the case that $L \ll \lambda_\Omega$, the sideband amplitudes in equations 1.60 and 1.61 agree with those found in equation 1.39, albeit with a minor difference in phase.

Chapter 2: Microwave photonics at the system level: I/Q down-conversion mixer with image rejection capability

In this chapter I will discuss the design and characterization of the microwave photonic I/Q down-conversion mixer described in [1]. I/Q down-conversion involves mixing of an incoming microwave signal at frequency f_{S} and a local oscillator (LO) at frequency f_0 to two outputs at intermediate frequency (IF) $f_{\mathrm{IF}} = |f_{\mathrm{S}} - f_0|$. These two outputs are copies that differ in phase by 90 degrees, and we refer to one as the in-phase (I) signal and the other as the quadrature (Q) signal.

2.1 Down-conversion

The primary advantage of down-converting microwave signals is easier digitization of the signal of interest. Additionally, down-conversion can be used to separate broadband microwave transmissions into smaller, lower-frequency channels for separate processing and digitization. While electrical down-conversion methods exist, microwave photonic mixers have many advantages over their electrical counterparts. As discussed in chapter 1, microwave photonic systems can make use of low-loss optical fiber transmission. This allows for the receiver to be located far from the signal processing location without incurring excessive loss from transmission over coaxial cable. Additionally, microwave photonic systems are much more resistant to electromagnetic

interference (EMI) and they boast wideband tunability and large instantaneous bandwidths.

Figure 2.1 shows schematic diagrams of three possible microwave photonic down-conversion techniques. While it is possible to achieve microwave photonic down-conversion using an optical

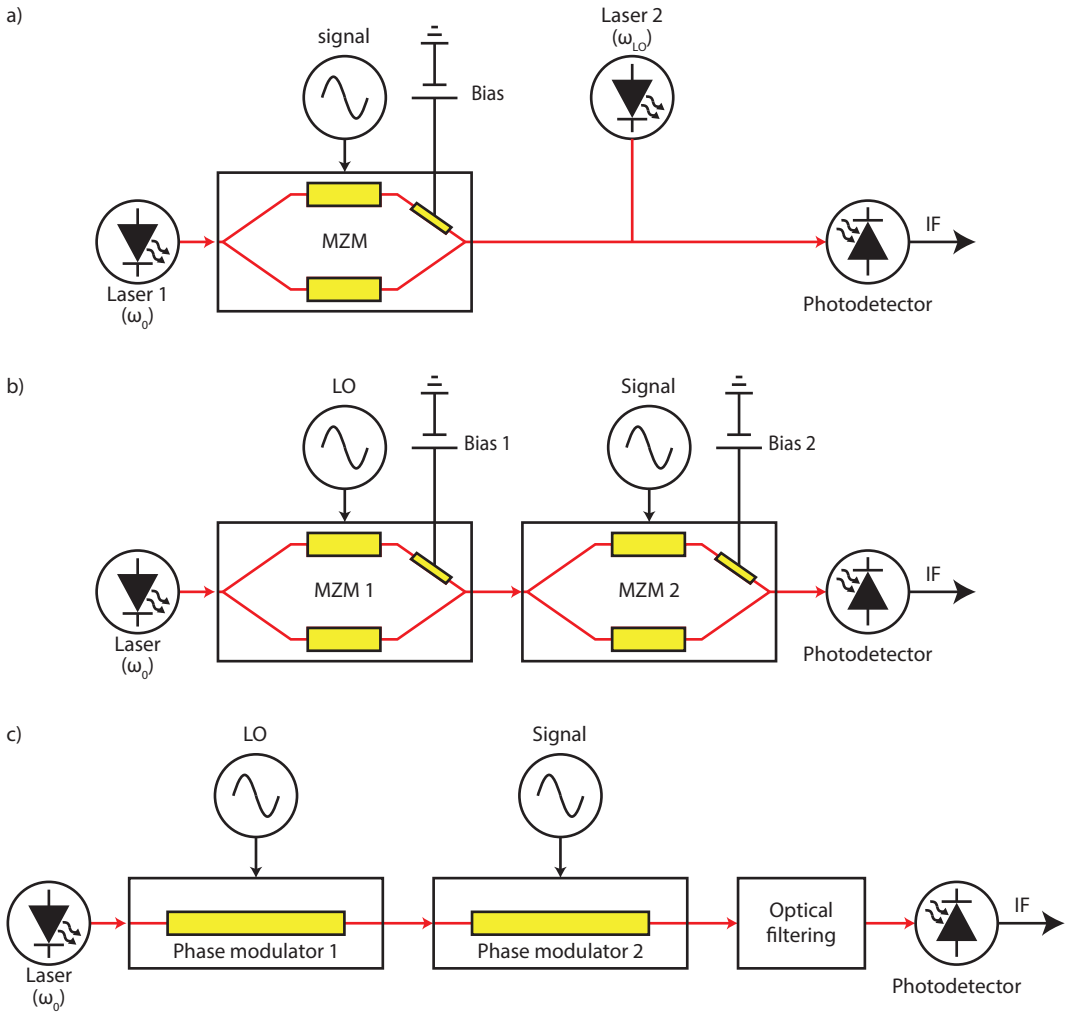

Figure 2.1: a) Schematic diagram of a microwave photonic down-conversion system utilizing an optical LO. b) Schematic diagram of a microwave photonic down-conversion system utilizing two cascaded MZMs. c) Schematic diagram of a microwave photonic down-conversion system utilizing two cascaded PMs.

local oscillator as shown in figure 2.1a, this technique requires two lasers that are carefully locked together. To avoid the need for locked lasers, it is possible to achieve microwave photonic down-conversion with a single laser by utilizing two Mach-Zehnder intensity modulators (MZMs) in

series [14] as shown in figure 2.1b or two MZMs in parallel followed by a balanced photodetector [15]. However these methods necessitate precise control of two bias voltages to ensure the two modulators are operating at the proper bias points. While it is possible to achieve single laser down-conversion with only a single MZM [16], this requires electrical addition of the signal and LO prior to modulation which can be difficult to achieve at high frequencies and bandwidths. To alleviate the need for carefully controlled bias voltages, down-conversion has also been achieved by two cascaded phase modulators followed by careful optical filtering [17] as shown in figure 2.1c.

More complex modulator structures have also been used to implement photonic down-conversion. Techniques have been reported using two I/Q modulators in parallel followed by digital signal processing [18, 19]. However these techniques require careful preparation of the signal and LO prior to modulation. Techniques for down-conversion using a single dual-drive Mach-Zehnder modulator (DDMZM) [20], or two DDMZMs in parallel [21] have also been demonstrated. In a DDMZM, rather than both arms of the device being driven by the same input, one arm is driven by the LO while the other is driven by the signal. As a result the device operates as two parallel phase modulators, with a relative phase delay controlled by the DDMZM bias point. Designs using dual-parallel Mach-Zehnder modulators (DPMZM), which behave similarly to two MZMs in parallel with a relative phase delay controlled by DC bias, have also been shown [22]. Microwave down-conversion mixers with phase shifting capability have also been demonstrated [23–25]. However, none of these systems address the image problem inherent to down-conversion processes.

2.1.1 The image problem and image rejection.

Figure 2.2a shows a schematic of the input and output spectra of a down-conversion mixer. Because the intermediate frequency is the absolute difference of the signal and LO frequencies,

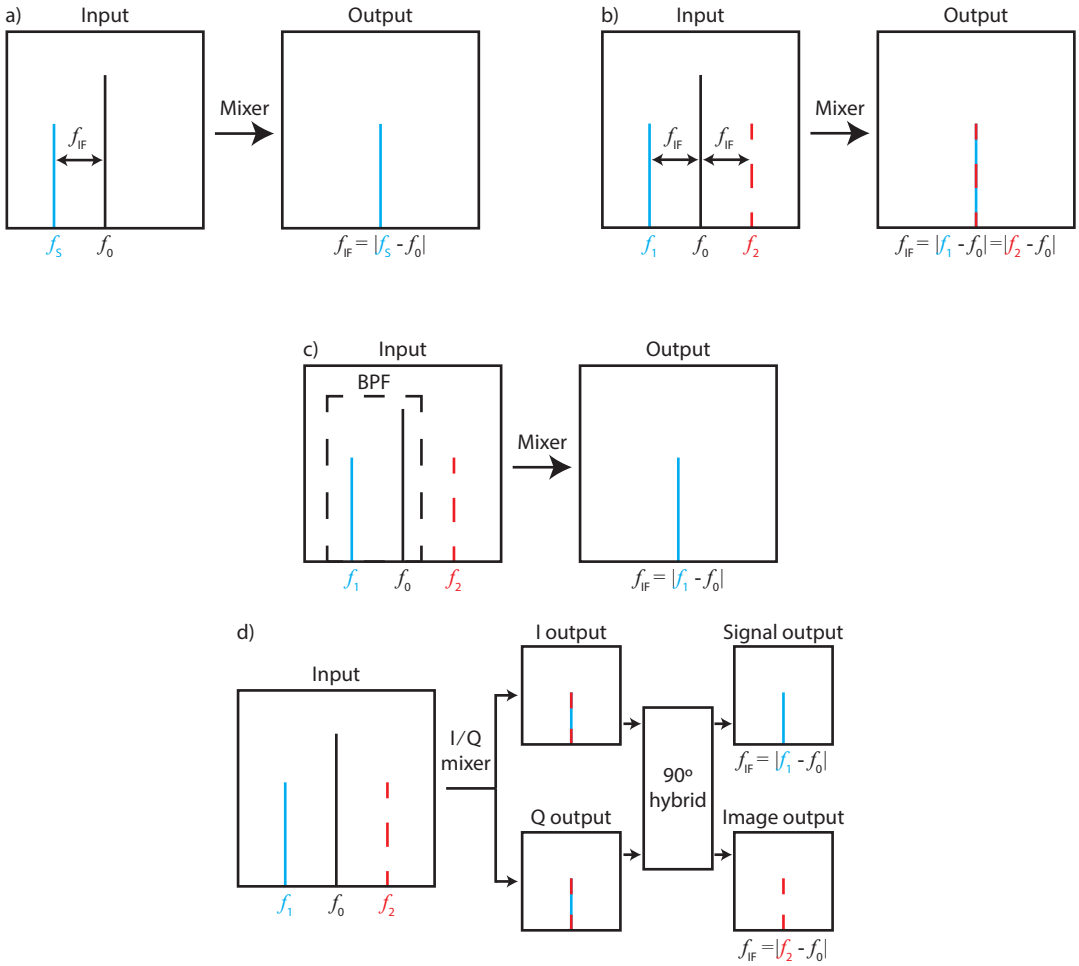

Figure 2.2: a) Schematic input and output spectra for a down-conversion mixer with only signal and LO present. b) Schematic input and output spectra for a down-conversion mixer with an image also present, showing interference at the output. c) Schematic input and output spectra for a down-conversion mixer showing a BPF that filters out the image. d) Schematic input and output spectra for an I/Q down-conversion mixer showing separation of the IF contributions from image and signal into separate outputs.

$f_{\rm IF} = |f_{\rm S} - f_0|$, there are two signal frequencies for any given LO that will produce the same IF

output:

$$f_1 = f_{\text{IF}} + f_0 \tag{2.1}$$

$$f_2 = f_{\text{IF}} - f_0 \tag{2.2}$$

where if f_1 is the frequency of the signal of interest we refer to f_2 as the image frequency and vice versa. Once overlapped in frequency at the output of the mixer as shown in figure 2.2b, contributions from the signal of interest and image can not be separated by filtering of the output. One solution to this problem is to simply use a band pass filter (BPF) at the microwave input to eliminate interference from the image as shown in figure 2.2c, but this method necessarily reduces the receiver bandwidth as only frequencies within the pass band can be down-converted. However, given I and Q outputs as shown in figure 2.2d, the well known Hartley architecture can be used to separate the contributions from the signal and image into separate outputs of a 90 degree electrical hybrid [26].

Several methods for microwave photonic I/Q down-conversion and image rejection have been reported [27]. A straightforward way to achieve this is to duplicate the microwave input and/or LO with a 90 degree phase shift added to one of the duplicates [17, 28, 29]. However, this method requires a 90 degree electrical phase shift at high frequencies, and necessarily increases system size, weight, and power consumption. Methods making use of multiple lasers have also been reported [30, 31], but these have the drawback of requiring careful simultaneous tuning of the two laser sources. Methods making use of a 90 degree optical hybrid have also been reported [32–37], which take advantage of balanced photodetection to reduce the effect of mixing spurs. Methods making use of a combination of polarization control and/or bias control have been

reported extensively [38–42], all of which require multiple carefully controlled set points.

2.2 Asymmetric Mach-Zehnder interferometer based down-conversion mixer with image rejection capability

In this section I will discuss in detail the mixer design reported in [1], which makes use of a single DDMZM followed by a band pass filter and asymmetric Mach-Zehnder interferometer. In principle this design requires only one carefully controlled bias point for operation, boasting reduced system complexity. Additionally, in [1] we demonstrated down-conversion and demodulation of a 1 Gbaud QPSK data modulated signal in the presence of a strong interfering image tone, confirming wideband operation.

2.2.1 Theory of operation

Fig. 2.3a shows a schematic diagram of the system design. Light from a laser source is

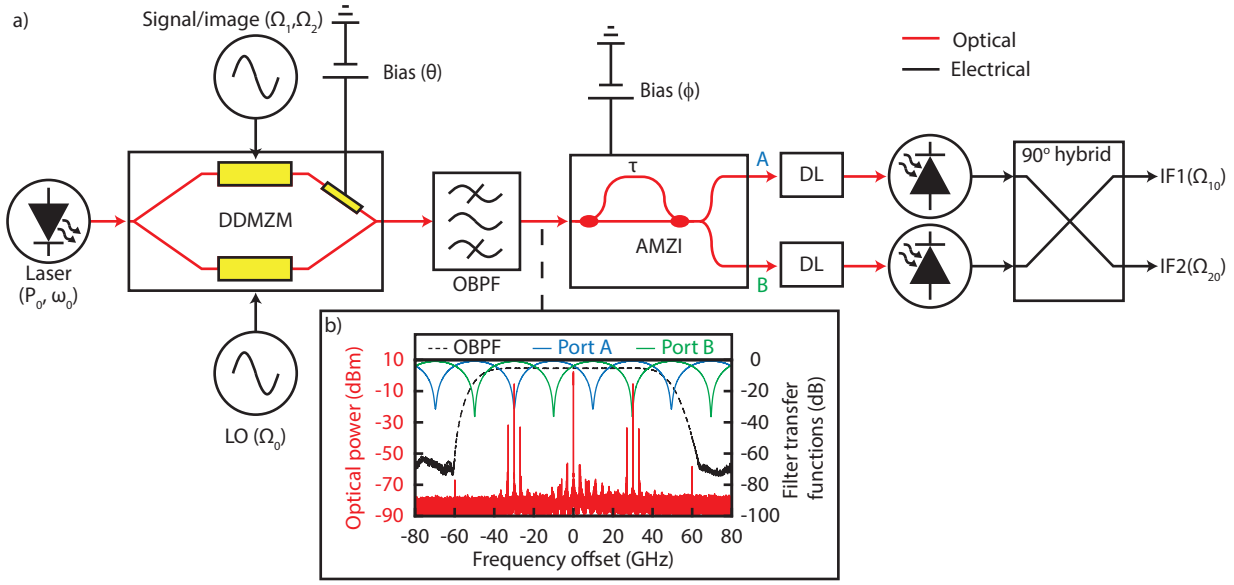

Figure 2.3: a) schematic diagram of the mixer system. b) optical spectrum at the output of the OBPF with OBPF and AMZI transfer functions overlaid. [1]

sent through a DDMZM, where the light is split evenly into two arms. In the lower arm the phase of the light is modulated by the microwave LO $V_{\text{lower}} = V_0 \sin(\Omega_0 t)$ where V_0 is the LO voltage at frequency $f_0 = \Omega_0/2\pi$, while in the upper arm it is modulated by the microwave signal and image $V_{\text{upper}} = V_1 \sin(\Omega_1 t) + V_2 \sin(\Omega_2 t)$ where V_1 is the signal voltage at frequency $f_1 = \Omega_1/2\pi$ and V_2 is the image voltage at frequency $f_2 = \Omega_2/2\pi$. A DC bias voltage applied to the upper arm induces an overall phase shift θ between the two arms before they are recombined at the output of the DDMZM. We define the optical field from the laser as $a_{\text{in}}(t) = \sqrt{P_0} e^{j\omega t}$ where P_0 is the optical power. We then describe the DDMZM output as follows:

$$a_{\text{DDMZM}}(t) = \underbrace{\frac{1}{\sqrt{2}}\begin{bmatrix}1 & j\end{bmatrix}}_{\text{combiner}} \underbrace{\begin{bmatrix} e^{j[m_1 \sin(\Omega_1 t) + m_2 \sin(\Omega_2 t) + \theta]} & 0 \\ 0 & e^{jm_0 \sin(\Omega_0 t)} \end{bmatrix}}_{\text{modulation}} \underbrace{\frac{1}{\sqrt{2}}\begin{bmatrix}1 \\ j\end{bmatrix}}_{\text{splitter}} a_{in}(t) \tag{2.3}$$

$$a_{\text{DDMZM}}(t) = \frac{\sqrt{P_0}}{2} e^{j\omega t} \left\{ e^{j[m_1 \sin(\Omega_1 t) + m_2 \sin(\Omega_2 t) + \theta]} - e^{jm_0 \sin(\Omega_0 t)} \right\} \tag{2.4}$$

where $m_i = \pi V_i / V_\pi$ is the modulation depth corresponding to each of the three inputs. Applying the Jacobi-Anger expansion to equation 2.4 yields

$$a_{\text{DD}}(t) = \frac{\sqrt{P_0}}{2} e^{j\omega t} \left[e^{j\theta} \sum_{k=-\infty}^{\infty} \sum_{\ell=-\infty}^{\infty} J_k(m_1) J_\ell(m_2) e^{j(k\Omega_1 + \ell\Omega_2)t} - \sum_{n=-\infty}^{\infty} J_n(m_0) e^{jn\Omega_0 t} \right] \tag{2.5}$$

where $J_n(m)$ is the n^{th} order Bessel function of the first kind. To reduce the effect of second order distortion on the output, an optical band pass filter (OBPF) immediately following the DDMZM extinguishes all frequencies in equation 2.5 with $|n| > 1$ or $|k + \ell| > 1$. If we further assume that $m_1, m_2 \ll 1$ we can expand the remaining terms in equation 2.5 to first order in m_1 and m_2,

yielding:

$$a_{\text{OBPF}}(t) = \frac{\sqrt{P_0}}{2} e^{j\omega t} \left[e^{j\theta} \left(1 + \frac{m_1}{2} e^{j\Omega_1 t} - \frac{m_1}{2} e^{-j\Omega_1 t} + \frac{m_2}{2} e^{j\Omega_2 t} - \frac{m_2}{2} e^{-j\Omega_2 t} \right) - \sum_{n=-1}^{1} J_n(m_0) e^{jn\Omega_0 t} \right] \tag{2.6}$$

Figure 2.3b shows the optical spectrum at the output of the OBPF, and the superposed black dashed curve shows the transfer function of the OBPF. After the OBPF, the light is passed through an asymmetric Mach-Zehnder interferometer (AMZI) fiber-delay filter. This splits the light into two paths, one of which is delayed by time τ before recombining them. The AMZI yields two complementary outputs A and B, the spectral transfer function of which are as follows:

$$t_A(\omega') = \sin\left[\frac{(\omega' - \omega)\tau + \phi}{2} \right] \tag{2.7}$$

$$t_B(\omega') = \cos\left[\frac{(\omega' - \omega)\tau + \phi}{2} \right] \tag{2.8}$$

where ϕ is controlled by a DC bias voltage. The power transmission $|t_i(\omega')|^2$ in each arm as a function of frequency is superposed in figure 2.3b. This power transmission is periodic in frequency with period $1/\tau$, which we refer to as the free spectral range (FSR) of the AMZI. The AMZI FSR and ϕ are then chosen such that $t_A(\omega + \Omega_0) = t_B(\omega - \Omega_0) = 1$, which directs the upper LO sideband to port A, and the lower LO sideband to port B. This is equivalent to imposing

the following conditions on ϕ and τ:

$$\phi = \frac{\pi}{2} \tag{2.9}$$

$$\Omega_0 \tau = \frac{\pi}{2} + 4\pi q \tag{2.10}$$

where q is some integer. The output optical field in each path can then be described as follows:

$$\begin{aligned} a_A(t) = \frac{\sqrt{P_0}}{2} e^{j\omega t} \Bigg\{ e^{j\theta} \Bigg[\frac{1}{\sqrt{2}} + \cos\left(\frac{\Omega_{10}\tau}{2}\right) \frac{m_1}{2} e^{j\Omega_1 t} + \sin\left(\frac{\Omega_{10}\tau}{2}\right) \frac{m_1}{2} e^{-j\Omega_1 t} \dots \\ + \cos\left(\frac{\Omega_{20}\tau}{2}\right) \frac{m_2}{2} e^{j\Omega_2 t} + \sin\left(\frac{\Omega_{20}\tau}{2}\right) \frac{m_2}{2} e^{-j\Omega_2 t} \Bigg] \dots \\ - \left[\frac{J_0(m_0)}{\sqrt{2}} + J_1(m_0) e^{j\Omega_0 t} \right] \Bigg\} \end{aligned} \tag{2.11}$$

$$\begin{aligned} a_B(t) = \frac{\sqrt{P_0}}{2} e^{j\omega t} \Bigg\{ e^{j\theta} \Bigg[\frac{1}{\sqrt{2}} - \sin\left(\frac{\Omega_{10}\tau}{2}\right) \frac{m_1}{2} e^{j\Omega_1 t} - \cos\left(\frac{\Omega_{10}\tau}{2}\right) \frac{m_1}{2} e^{-j\Omega_1 t} \dots \\ - \sin\left(\frac{\Omega_{20}\tau}{2}\right) \frac{m_2}{2} e^{j\Omega_2 t} - \cos\left(\frac{\Omega_{20}\tau}{2}\right) \frac{m_2}{2} e^{-j\Omega_2 t} \Bigg] \dots \\ - \left[\frac{J_0(m_0)}{\sqrt{2}} - J_1(m_0) e^{-j\Omega_0 t} \right] \Bigg\} \end{aligned} \tag{2.12}$$

where $\Omega_{10} \equiv \Omega_1 - \Omega_0$ and $\Omega_{20} \equiv \Omega_2 - \Omega_0$ represent the angular frequencies of the down-converted signal and image, respectively. photodetection of $a_A(t)$ and $a_B(t)$ produces photocurrents at

frequency Ω_{10} and Ω_{20}:

$$i_A(t) = \frac{-RP_0J_1(m_0)}{4}\left[m_1\cos\left(\frac{\Omega_{10}\tau}{2}\right)\cos\left(\Omega_{10}t+\theta\right)\ldots\right.$$
$$\left.+\, m_2\cos\left(\frac{\Omega_{20}\tau}{2}\right)\cos\left(\Omega_{20}t+\theta\right)\right] \tag{2.13}$$
$$i_B(t) = \frac{-RP_0J_1(m_0)}{4}\left[m_1\cos\left(\frac{\Omega_{10}\tau}{2}\right)\cos\left(\Omega_{10}t-\theta\right)\ldots\right.$$
$$\left.+\, m_2\cos\left(\frac{\Omega_{20}\tau}{2}\right)\cos\left(\Omega_{20}t-\theta\right)\right] \tag{2.14}$$

where R is the photodetector responsivity and we have omitted terms that do not oscillate at either Ω_{10} or Ω_{20}. If we assume that Ω_1 and Ω_2 are spaced evenly to either side of Ω_0, that is $\Omega_1 - \Omega_0 = \Omega_0 - \Omega_2 = \Omega_{\text{IF}}$ we obtain

$$i_A(t) = \frac{-RP_0J_1(m_0)}{4}\cos\left(\frac{\Omega_{\text{IF}}\tau}{2}\right)\left[m_1\cos\left(\Omega_{\text{IF}}t+\theta\right)+m_2\cos\left(\Omega_{\text{IF}}t-\theta\right)\right] \tag{2.15}$$
$$i_B(t) = \frac{-RP_0J_1(m_0)}{4}\cos\left(\frac{\Omega_{\text{IF}}\tau}{2}\right)\left[m_1\cos\left(\Omega_{\text{IF}}t-\theta\right)+m_2\cos\left(\Omega_{\text{IF}}t+\theta\right)\right] \tag{2.16}$$

The terms in equations 2.15 and 2.16 that are proportional to m_1 represent the down-converted signal, while the terms proportional to m_2 represent the down-converted image which is down-converted to the same IF frequency. Here we can see that the phase of the down-converted signal in $i_A(t)$ leads its counterpart in $i_B(t)$ by 2θ, where the down-converted image lags behind by the same amount. If we choose $\theta = \pi/4$, these components will be 90 degrees out of phase, yielding I and Q photocurrents at the IF. Passing $i_A(t)$ and $i_B(t)$ through a 90 degree electrical hybrid, we

obtain two output currents (IF1,IF2):

$$\text{IF1} = \frac{1}{\sqrt{2}}[i_A(t) + i'_B(t)] \tag{2.17}$$

$$\text{IF2} = \frac{1}{\sqrt{2}}[i'_A(t) + i_B(t)] \tag{2.18}$$

where we have chosen $\theta = \pi/4$ and

$$i'_A(t) = \frac{-RP_0J_1(m_0)}{4}\cos\left(\frac{\Omega_{\text{IF}}\tau}{2}\right)\left[m_1\cos\left(\Omega_{\text{IF}}t + \frac{3\pi}{4}\right) + m_2\cos\left(\Omega_{\text{IF}}t + \frac{\pi}{4}\right)\right] \tag{2.19}$$

$$i'_B(t) = \frac{-RP_0J_1(m_0)}{4}\cos\left(\frac{\Omega_{\text{IF}}\tau}{2}\right)\left[m_1\cos\left(\Omega_{\text{IF}}t + \frac{\pi}{4}\right) + m_2\cos\left(\Omega_{\text{IF}}t + \frac{3\pi}{4}\right)\right] \tag{2.20}$$

Then at the output of the hybrid we have

$$\text{IF1}(t) = \frac{-\sqrt{2}RP_0J_1(m_0)}{4}\cos\left(\frac{\Omega_{\text{IF}}\tau}{2}\right)m_1\cos\left(\Omega_{\text{IF}}t + \frac{\pi}{4}\right) \tag{2.21}$$

$$\text{IF2}(t) = \frac{-\sqrt{2}RP_0J_1(m_0)}{4}\cos\left(\frac{\Omega_{\text{IF}}\tau}{2}\right)m_2\cos\left(\Omega_{\text{IF}}t + \frac{\pi}{4}\right) \tag{2.22}$$

Here we see that only the signal contributes to IF1, while only the image contributes to IF2. It is useful to compare the output signal photocurrent to the theoretical output photocurrent at some frequency f_{MZM} produced by a non-down-converting microwave photonic system consisting of a quadrature-biased MZM modulated at f_{MZM} with modulation depth m_1 and utilizing direct detection:

$$i_{\text{MZM}}(t) = \frac{RP_0m_1}{2}\cos(\Omega_{\text{MZM}}t) \tag{2.23}$$

The gain of our system compared to the MZM is as follows:

$$\frac{G}{G_{\text{MZM}}} = \frac{1}{2}\left[J_1(m_0)\cos\left(\frac{\Omega_{\text{IF}}\tau}{2}\right)\right]^2 \tag{2.24}$$

This is maximized when $m_0 = 1.841$, and takes on a value of approximately -7.96 dB for an IF of 3 GHz.

2.2.2 System characterization

To characterize the system performance, a tunable laser at 1552.525 nm is sent in to the optical input of a DDMZM (Sumitomo Osaka Cement T.DEH1.5-40-ADC). The upper arm of the DDMZM is modulated by the microwave signal and/or image while the lower arm is modulated by the LO, and a DC power supply is connected to the DC bias electrode. The output of the DDMZM is then passed through a Finisar Waveshaper 1000s which is configured as an OBPF with a bandwidth of 95 GHz as shown in figure 2.3b. The output of the OBPF is then split by an AMZI (Avensys Tech DPSK demodulator DPSK4000S30) with an FSR of 40 GHz. Each arm of the AMZI is separately photodetected, and optical delay lines in each arm equalize the path lengths on the order of the IF frequency prior to photodetection. Here we note that while the AMZI used in this experiment accepts a DC bias voltage (ϕ) for thermal stabilization, passively stable AMZI filters are commercially available, and the use of a passively stable AMZI would reduce the number of required bias voltages to one. The two output photocurrents are then combined in a 90 degree electrical hybrid (Narda 4356B) which has a nominal operating frequency range of 2-18 GHz, and nominal phase and amplitude imbalances of ± 7 degrees and ± 0.75 dB respectively.

To measure the image rejection capability of the system, a LO at $f_0 = 30$ GHz was used to simultaneously down-convert a signal tone at $f_1 = 26.99975$ GHz and an image tone at $f_2 = 32.99975$ GHz. Figure 2.4a shows the measured input LO and signal/image spectra superposed. Figure 2.4b shows the output IF spectra (averaged over 100 traces) for $\theta = 45°$ and $\theta = -45°$. In

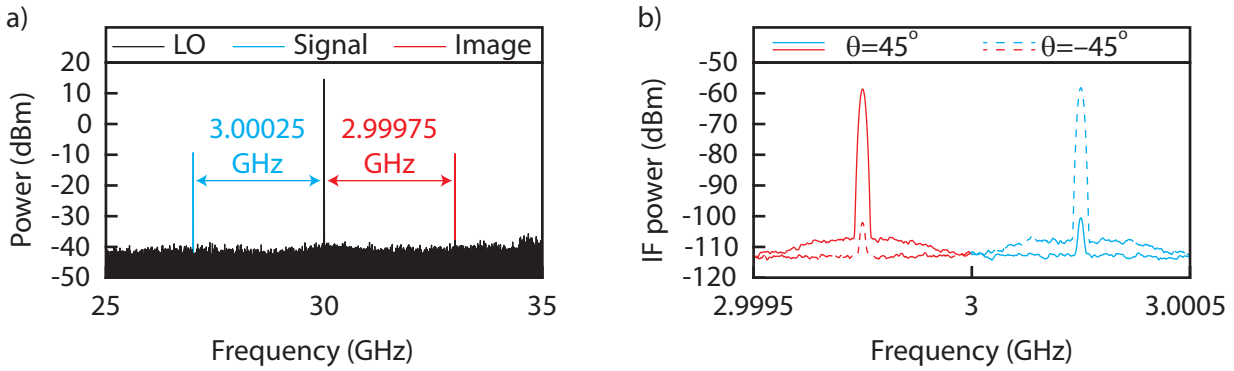

Figure 2.4: a) Measured input LO and signal/image spectra superposed. b) Measured output IF spectra (averaged over 100 traces). When $\theta = 45°$ the signal is suppressed by over 40 dB relative to the image, and when $\theta = -45°$ the image is likewise suppressed relative to the signal. [1]

the $\theta = 45°$ case the contribution from the image is over 40 dB stronger than the signal while in the $\theta = -45°$ case the contribution from the signal is over 40 dB stronger than the image. Thus by tuning θ we can obtain just signal or image with over 40 dB of isolation.

To verify the response of the system as a function of LO strength, the relative IF gain $\frac{G}{G_{\text{MZM}}}$ was measured as a function of LO modulation depth m_0 for LO frequencies of $f_0 = 10$ GHz and $f_0 = 30$ GHz. The signal in frequency in both cases was tuned to produce an IF at 3 GHz. To eliminate the effect of the modulator DC bias, this measurement was performed prior to combination in the electrical 90 degree hybrid by examining only one of the two photocurrents. Figure 2.5a shows the data with theoretical calculations for the response both before and after the hybrid superposed. Because the V_π of the modulator increases with frequency, the modulation depth at 30GHz is limited to a maximum of 1.3 radians, determined by the maximum output

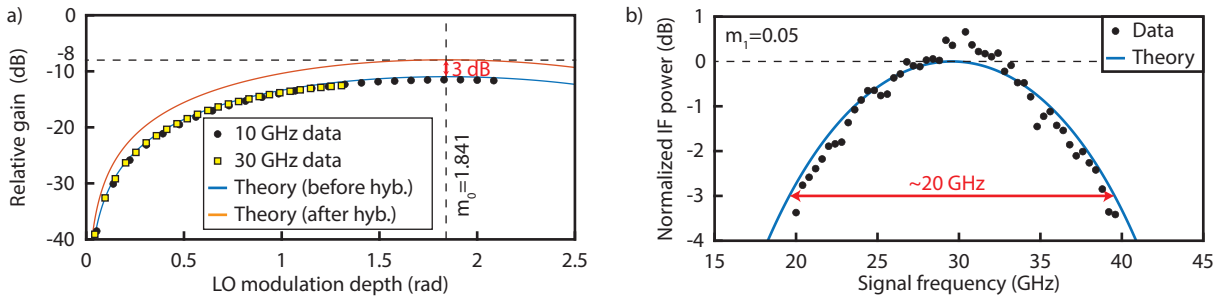

Figure 2.5: a) Relative gain G/G_{MZM} of a 3 GHz IF output as a function of LO modulation depth m_0 for LO frequencies of $f_0 = 10$ GHz and $f_0 = 30$ GHz, with theoretical calculations for before and after combination in the 90 degree electrical hybrid superposed. b) Normalized output IF power vs signal frequency for a fixed LO frequency of $f_0 = 30$ GHz and fixed modulation depths of $m_0 = 1.3$ and $m_1 = 0.05$. [1]

power of our signal generator (19.5 dBm). However, in both cases the measured relative gain agrees closely with the calculated response shown by the blue curve. To measure the response of the system as a function of signal frequency the LO was fixed at $f_0 = 30$ GHz and $m_0 = 1.3$ and the signal frequency f_1 was varied while the signal modulation depth was held constant at $m_1 = 0.05$. Figure 2.5b shows the normalized IF output power as a function of signal frequency f_1 with theoretical calculations superposed, showing a $\cos^2\left(\frac{\Omega_{\text{IF}}\tau}{2}\right)$ dependence and a 3dB bandwidth of approximately $1/2\tau = 20$ GHz, determined by the FSR of the AMZI. We expect the image rejection bandwidth of the system depends strongly on the particular electrical hybrid used at the output.

To evaluate linearity of the system as a function of signal power, the signal arm is modulated by two closely spaced tones at $f_1 = 26.99975$ GHz and $f_2 = 27.00025$ GHz while the LO is fixed at $f_0 = 30$ GHz and $m_0 = 1.3$. The powers of the IF outputs at frequencies $(f_0 - f_1)$ and $(f_0 - f_2)$, the second order products at frequencies $2(f_0 - f_1)$, $2(f_0 - f_2)$, and $(2f_0 - f_1 - f_2)$, and the third order intermodulation distortion products (IMD3) at frequencies $(f_0 - 2f_1 - f_2)$ and $(f_0 - f_1 - 2f_2)$ are then measured as a function of the input signal power. Figure 2.6 shows the results of this

measurement, indicating that the IMD3 dominates for any system with a bandwidth of over 4 MHz, yielding a spurious free dynamic range (SFDR) of 100.6 dB-Hz$^{2/3}$. The system noise floor is primarily dominated by thermal noise under the measurement conditions. Measurements of the second order distortion were taken with and without the OBPF in place, showing that the OBPF is crucial in reducing the effect of second order products originating from the second order optical modulation sidebands. With the filter in place, the second order distortion is limited by electrical cross talk in the modulator, which produces optical tones at $\omega \pm (\Omega_0 - \Omega_1)$ and $\omega \pm (\Omega_0 - \Omega_2)$, which beat with the tones at $\omega \pm \Omega_1$ and $\omega \pm \Omega_2$. These tones reside within the first order optical sidebands and are therefore not removed by the OBPF.

2.2.3 Broadband operation

To confirm the broadband capability of the system, a signal consisting of a 1 Gbaud QPSK pseudo-random bit sequence (PRBS11) with a center frequency of $f_1 = 26.99975$ GHz and average power of -10 dBm was used as the signal of interest, while a strong tone at $f_2 = 32.00025$ GHz and 0 dBm was used as the image. Again the LO was fixed at $f_0 = 30$ GHz and $m_0 = 1.3$, and the electrical output was then amplified 58 dB before being detected by a spectrum analyzer and an 8GHz real time oscilloscope. The oscilloscope traces were processed offline to recover the QPSK constellation at the output. Figure 2.7a shows the case where the measurement was taken before the electrical hybrid. In this case, the contribution to the output from the image tone can be clearly seen in the spectral measurement and the constellation is completely distorted. Figure 2.7b shows the measurement after the hybrid, where the image is rejected. Here we no longer see the spectral contribution from the image, and the constellation can be clearly recovered with an

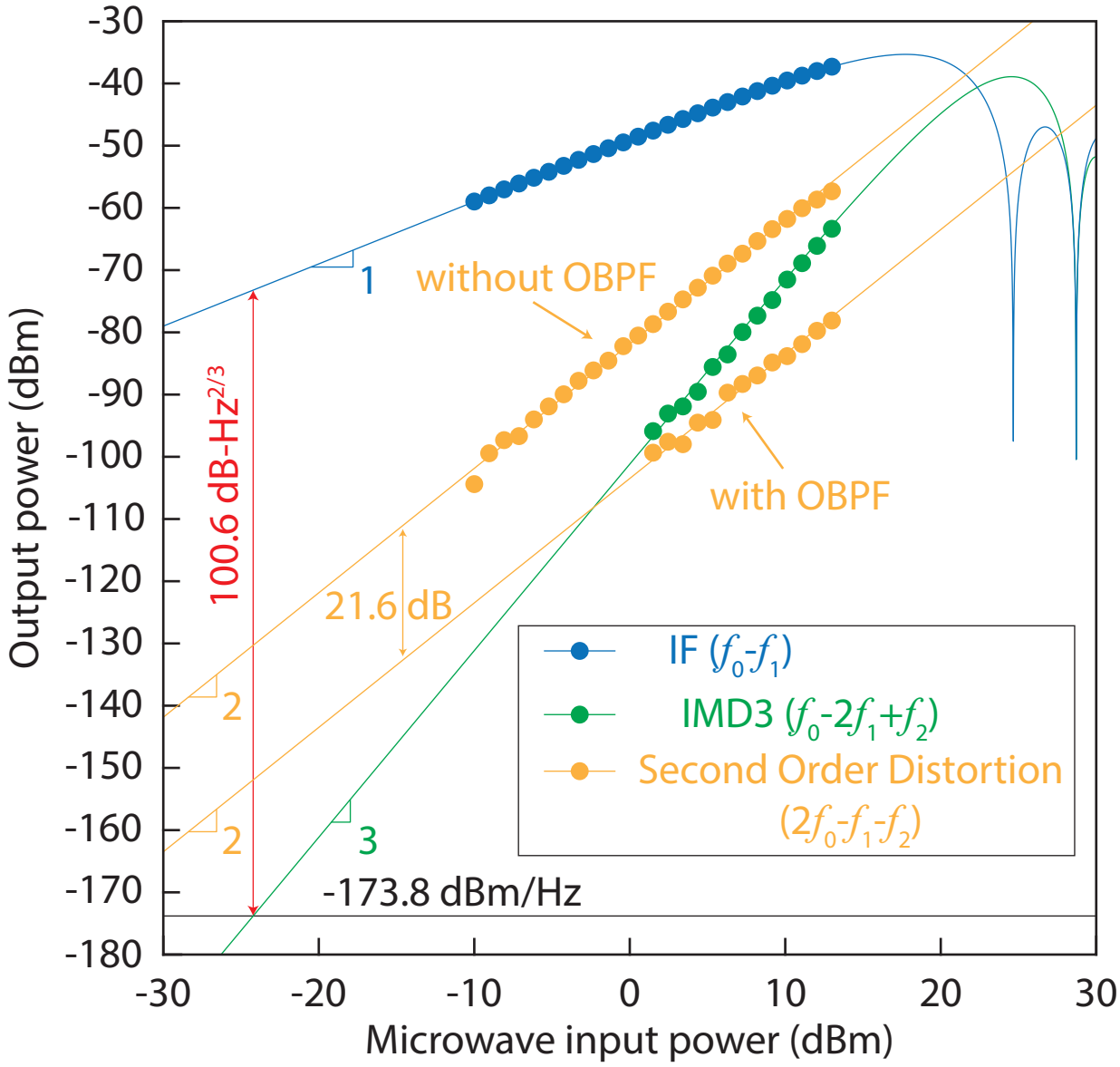

Figure 2.6: Measurement of the linearity of the system for equal strength input tones at $f_1 = 26.99975$ GHz and $f_2 = 27.00025$ GHz and fixed LO at $f_0 = 30$ GHz and $m_0 = 1.3$, indicating an SFDR of 100.6 dB-Hz$^{2/3}$. Solid lines indicate fits to the data: the IF and IMD3 were fit to theoretical calculations, while the second order distortions were fit to lines of slope 2. [1]

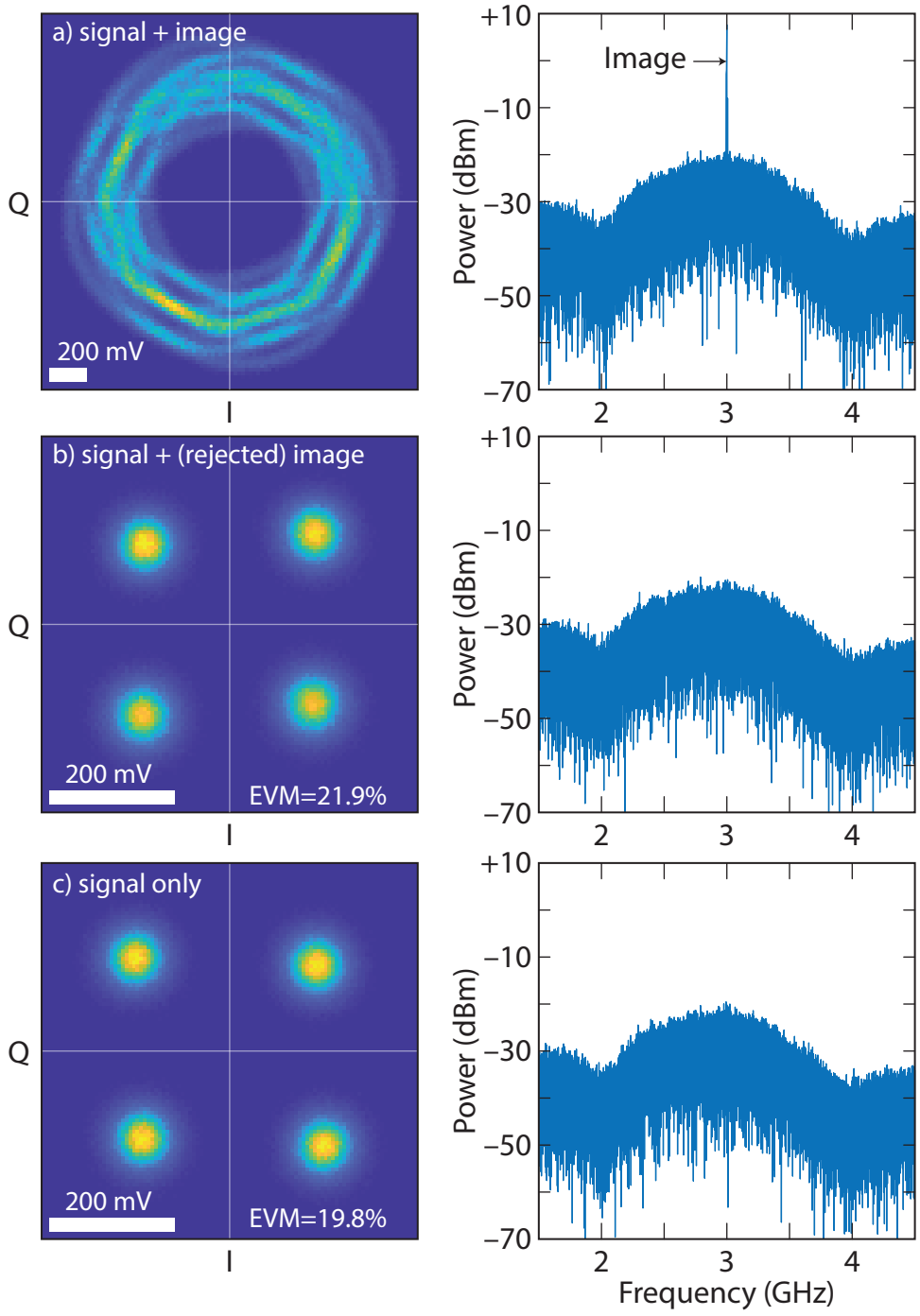

Figure 2.7: a) Output constellation and spectrum measured before the electrical hybrid, where contributions from the signal and image are both present. b) Output constellation and spectrum measured after the hybrid for the case where the image is rejected. c) Output constellation and spectrum measured after the hybrid for the case that the image was not present at the input. [1]

error vector magnitude (EVM) of 21.9%. For comparison, figure 2.7c shows the measurement after the hybrid in the case where the image was not present at the system input, yielding an EVM of 19.8%. This indicates that the presence of the rejected image only slightly degrades the signal.

2.2.4 Conclusions

Here I have presented a simple microwave photonic down-converting I/Q mixer that is capable of over 40 dB of image rejection. The system in this experiment requires only two bias voltages to be controlled, which can in principle be reduced to only one with an appropriate choice of AMZI. Additionally the system requires only one laser and one modulator, and the theoretical gain of the system is only 7.96 dB lower than that of a direct non-down-converting MZM microwave photonic link. The system has a 3dB IF bandwidth of 20 GHz limited by the AMZI FSR, and we show down-conversion and demodulation of 1 Gbaud QPSK data even in the presence of an image tone that is 10 dB higher than the average QPSK power. This demonstrates the wideband performance of the system while emphasizing the effectiveness of the image rejection capability.

Chapter 3: Microwave photonics at the device level: doubly-resonant metal-free microwave receiver in aluminum nitride

In this chapter, I will discuss the design, fabrication, and characterization of an integrated photonic microwave receiver that takes advantage of two resonant structures: one for the optical carrier and one for the microwave signal. Aluminum nitride (AlN) is chosen as the electro-optic material for this device, taking advantage of the relative ease of growth and fabrication as compared to other electro-optic materials like lithium niobate. Additionally, the large band gap of AlN enables its use in the ultraviolet as well as the mid-infrared [43]. Highly c-axis aligned AlN thin films can be grown via metal-organic chemical vapor deposition (MOVCD) [44] or RF magnetron sputtering [45, 46], and the use of AlN as a piezoelectric material has led to the maturation of established fabrication techniques. A ring resonator structure fabricated in the AlN serves as the optical resonator, and the optical behavior of ring resonators is well understood [47]. Ring resonators are typically characterized by their quality factor (Q), which is defined as the resonant frequency divided by the full width at half max (FWHM) of the resonance, their free spectral range (FSR) which is the spacing between resonant frequencies, and their finesse $\mathcal{F} = \frac{\text{FSR}}{\text{FWHM}}$. The quality factor is usually limited by the propagation loss in the ring, where the FSR is determined by the ring perimeter and group velocity.

A dielectric resonator antenna (DRA) serves as the microwave resonator. DRAs consist of

dielectric structures with high relative permittivity (ϵ_r), which may be designed to act as resonant cavities at microwave frequencies. DRAs have advantages over traditional conducting antennas, such as smaller size due to their high ϵ_r and absence of conducting losses at frequencies in the tens to hundreds of GHz [48]. Additionally, DRAs are non-metallic structures, facilitating the design of entirely metal-free devices which are inherently less susceptible to damage or interference from high power electromagnetic pulses than their counterparts consisting of small metallic components. DRAs are often placed upon a ground plane, which forces certain symmetries and therefore affects which resonant modes are possible for a given DRA/ground plane structure [49]. One challenge associated with DRA use is the inability to electrically couple the DRA to a standard terminated transmission line or load impedance. As a result the DRA is often fed by means such as microstrip transmission line or coaxial probe, where the field nearby the microstrip or probe is used to excite the DRA. The position of the feed point is chosen depending on the desired DRA mode [50]. In the work described in this chapter, the near field of the DRA resonant mode is excited by incident microwave radiation and is directly used to modulate light in an AlN resonator, alleviating the need for coupling to metallic structures.

Doubly-resonant AlN modulator structures using superconducting resonant microwave electrodes have been demonstrated [51], as have doubly-resonant modulators using a bulk lithium niobate whispering gallery mode resonator and a DRA [52, 53]. The lithium niobate and DRA structures described in [52, 53] have the additional advantage of being completely metal-free, increasing their immunity to electromagnetic attack as compared to devices with conventional conducting antennas. However, the lithium niobate whispering gallery mode resonator used in [52, 53] consists of a polished disk of lithium niobate which is coupled to laser light via a prism. This imposes significant limitations on size, weight, and stability compared to integrated

optical ring resonator devices. The doubly-resonant device described later in this chapter makes use of a DRA and an integrated optical AlN ring resonator to achieve metal-free doubly-resonant on-chip detection of free space microwave radiation.

3.1 Aluminum nitride electro-optics

In addition to its piezoelectric properties, AlN has a significant electro-optic response. AlN belongs to the hexagonal 6mm crystal symmetry group, which restricts its electro-optic tensor to only 6 non-zero elements, which can be described by 3 unique coefficients (see table 1.1):

$$r_{33}$$

$$r_{13} = r_{23}$$

$$r_{51} = r_{42}$$

Unlike in lithium niobate where r_{33} is largest non-zero element by a significant margin, in AlN r_{33} and r_{13} are approximately equal [54]. This, combined with the c-axis orientation of the sputtered AlN thin films, allows us to make use of the in-plane polarized (TE) optical mode without diminishing the electro-optic response. This is advantageous as low-loss TE mode waveguides are easier to fabricate since they can be made from thinner films than their out-of-plane polarized (TM) mode counterparts. This is because as the waveguide becomes thinner, the TM mode becomes less confined to the waveguide core than the TE mode as shown in figure 3.1, leading to more scattering from defects in the core-cladding interface. Since we expect this defect induced scattering to be the primary source of loss in the waveguide, the TM mode in this case tends to

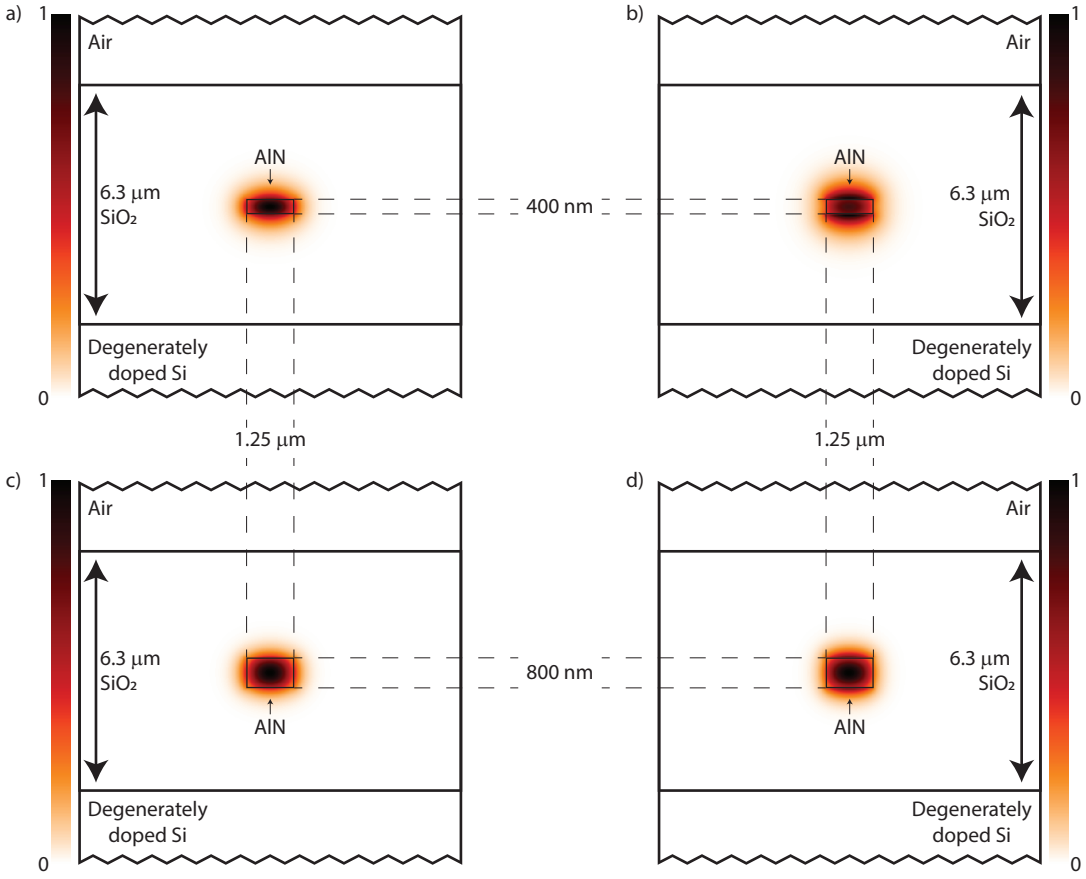

Figure 3.1: Schematic diagrams of two AlN waveguide structures with the magnitude of the simulated TE or TM electric field superposed. a) TE mode, 69.96% of power confined to the core. b) TM mode, 56.91% of power confined to the core. c) TE mode, 90.43% of power confined to the core. d) TM mode, 90.67% of power confined to the core. Simulations performed by Ansys Lumerical MODE finite difference eigenmode solver.

have higher loss. The TM loss can be improved by designing thicker waveguides, but in practice thicker waveguides are more challenging to fabricate due to limitations in etch masking and sidewall angle/roughness. Despite these challenges, electro-optic modulators in AlN have been demonstrated for both TE and TM optical modes [55, 56].

Ring resonators in AlN have been used for a variety of integrated photonic applications, and AlN rings with quality factors as high as 2.5 million in the telecom C-band have been demonstrated [57]. Electro-optic modulation at gigahertz frequencies has been shown using AlN ring resonators [12], as has high efficiency second harmonic generation [58, 59]. AlN optomechanical ring structures have also been demonstrated with mechanical mode frequencies in the gigahertz [60]. Photon pair sources using AlN rings for parametric down conversion have also been demonstrated [61], as have frequency comb generators using AlN ring resonators [62–64]. Choosing AlN as the electro-optic material for our devices enables CMOS-compatible fabrication of low-loss TE-mode ring resonators with a significant electro-optic response.

3.2 Doubly-resonant metal-free microwave photonic receiver

I will now discuss the design, fabrication, and characterization of an entirely metal-free, doubly-resonant, integrated photonic microwave receiver. Figure 3.2 shows a schematic diagram of the device, which consists of a half-cylinder DRA placed in close proximity to an on-chip integrated AlN ring resonator.

Careful choice of the DRA shape and AlN thin film substrate allow efficient overlap of the DRA near field on resonance and the resonant optical mode in the AlN resonator. In order to discuss the expected response of the device, I will first consider the theoretical propagation of

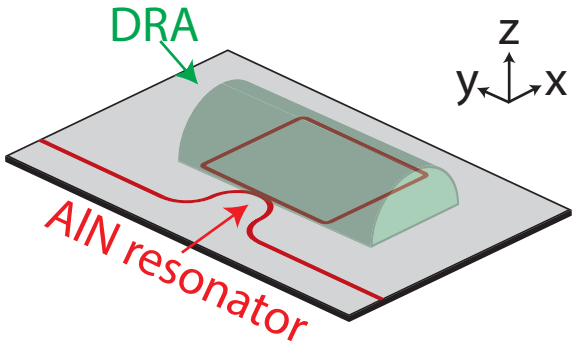

Figure 3.2: Schematic diagram of the doubly-resonant device

light in an electro-optic ring resonator in the presence of an external microwave electric field. I will then discuss the design and simulation of the DRA structure, followed by the AlN ring resonator design and fabrication. Finally, I will discuss the performance of the doubly-resonant device.

3.2.1 Theory of operation

The goal of this section is to understand the behavior of light traveling in an AlN ring resonator under the effect of a sinusoidally oscillating microwave electric field. We begin with a racetrack ring resonator in AlN like the one shown in figure 3.3, and electric field at the input of the directional coupler which is linearly polarized in the xy plane:

$$E_A = \frac{1}{2}(f(\mathbf{r}_\perp)A_0 e^{j\omega_0 t} + C.C.) \tag{3.1}$$

where $f(\mathbf{r}_\perp)$ describes the transverse eigenmode of the AlN waveguide and $\mathbf{r}_\perp$ is the position in the plane perpendicular to the plane of propagation. We will assume $f(\mathbf{r}_\perp)$ is normalized such that it's integral over the transverse plane is unity: $\int_{\mathbf{r}_\perp} |f(\mathbf{r}_\perp)|^2 dA = 1$. We will also assume that there is a microwave electric field acting over the ring path that in uniform with respect to $\mathbf{r}_\perp$ and

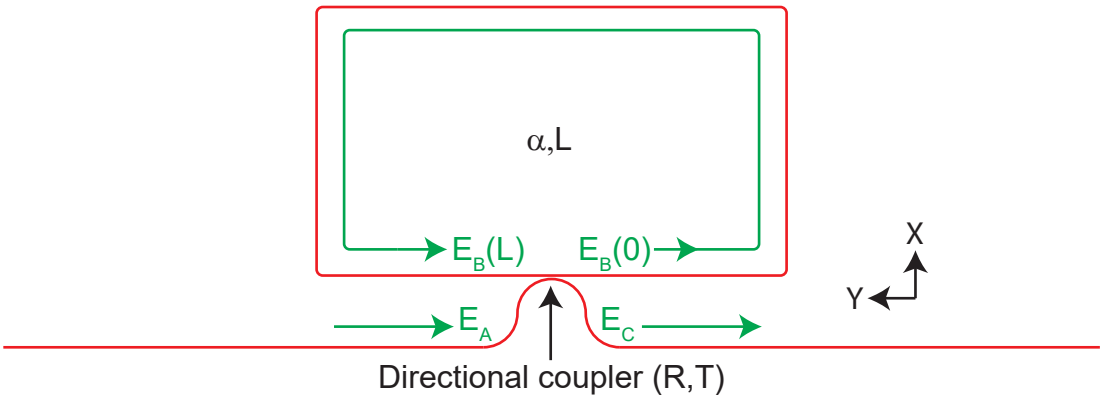

Figure 3.3: Schematic of ring resonator, showing locations of the fields and the directions of propagation. The red lines represent the optical waveguides that make up the resonator. R: directional coupler reflection coefficient, T: directional coupler transmission coefficient, α: field attenuation coefficient (nepers/meter), L: ring perimeter length

polarized in the z (out-of-plane) direction:

$$E_\Omega = A_\Omega(s)\sin(\Omega t + \phi) = \frac{1}{2}(-jA_\Omega(s)e^{(j\Omega t+\phi)} + C.C.) \tag{3.2}$$

where s is the distance traveled along the ring. Inside the ring, we will assume the following form for E_B:

$$E_B(s) = \frac{1}{2}\left\{f(\mathbf{r}_\perp)\left[B_0(s)e^{j(\omega_0 t-\kappa_0 s)} + B_+(s)e^{j(\omega_+ t-\kappa_+ s)} + B_-(s)e^{j(\omega_- t-\kappa_- s)}\right] + C.C.\right\}e^{-\alpha s} \tag{3.3}$$

where $\omega_\pm = \omega_0 \pm \Omega$, α is the field attenuation coefficient (nepers/meter), and $\kappa_{0,\pm} = \omega_{0,\pm} n_{\text{eff}}(\omega_{0,\pm})/c$ where $n_{\text{eff}}(\omega_{0,\pm})$ is the mode effective index. We will further assume that $B_{0,\pm}(s)$ are slowly varying and that the extraordinary axis of AlN is oriented in the z direction. Thus $\kappa_{0,\pm}$ is unchanged as the direction of propagation changes to follow the ring, so long as the E-field polarization remains in the xy plane. Finally, we will assume an output field of the form

$$E_C = \frac{1}{2}\left\{ f(\mathbf{r}_\perp)\left[C_0 e^{j\omega_0 t} + C_+ e^{j\omega_+ t} + C_- e^{j\omega_- t} \right] + C.C. \right\} \tag{3.4}$$

Assuming steady state, the directional coupler mixes the fields inside and outside the ring according to the following transfer function:

$$\begin{bmatrix} E_B(0) \\ E_C \end{bmatrix} = \begin{bmatrix} \sqrt{R} & j\sqrt{T} \\ j\sqrt{T} & \sqrt{R} \end{bmatrix} \begin{bmatrix} E_B(L) \\ E_A \end{bmatrix} \tag{3.5}$$

Where R is the coupler reflection coefficient, T is the coupler transmission coefficient, and L is the total path length around the ring. We assume that T and R are real, and that the coupler is lossless implying that $T + R = 1$.

We will now consider the effect of the external microwave field acting on $E_B(s)$. Following our analysis in Chapter 1 we arrive at the following equation:

$$\begin{aligned} \left(\nabla_\perp + \frac{\omega_i^2 \epsilon_r(\mathbf{r}_\perp, \omega_i)}{c^2} \right) f(\mathbf{r}_\perp) B_i(s) e^{-j\kappa_i s - \alpha s} &= (\kappa_i - j\alpha)^2 f(\mathbf{r}_\perp) B_i(s) e^{-j\kappa_i s - \alpha s} \ldots \\ &\quad + 2j(\kappa_i - j\alpha) f(\mathbf{r}_\perp) \frac{\partial B_i(s)}{\partial s} e^{-j\kappa_i s - \alpha s} \ldots \\ &\quad - \omega_i^2 \mu_0 P_i^{(2)}(\mathbf{r}_\perp, s) \end{aligned} \tag{3.6}$$

where $i \in \{0, +, -\}$, we have neglected the $\frac{\partial^2 B_i(s)}{\partial s^2}$ term under the assumption that $B_i(s)$ is

slowly varying, and $P_i^{(2)}(\mathbf{r}_\perp, s)$ is the second order polarization oscillating at ω_i:

$$P_0^{(2)}(\mathbf{r}_\perp, s) = \frac{j\epsilon_0 n_0^4}{2} r_{13}(\mathbf{r}_\perp) f(\mathbf{r}_\perp) \left[A_\Omega(s) B_-(s) e^{-j\kappa_- s} - A_\Omega^*(s) B_+(s) e^{-j\kappa_+ s} \right] e^{-\alpha s} \tag{3.7}$$

$$P_+^{(2)}(\mathbf{r}_\perp, s) = \frac{j\epsilon_0 n_0^4}{2} r_{13}(\mathbf{r}_\perp) f(\mathbf{r}_\perp) A_\Omega(s) B_0(s) e^{-j\kappa_0 s - \alpha s} \tag{3.8}$$

$$P_-^{(2)}(\mathbf{r}_\perp, s) = \frac{-j\epsilon_0 n_0^4}{2} r_{13}(\mathbf{r}_\perp) f(\mathbf{r}_\perp) A_\Omega^*(s) B_0(s) e^{-j\kappa_0 s - \alpha s} \tag{3.9}$$

Here n_0 is the ordinary refractive index of the AlN thin film at ω_0 and we have assumed that $\Omega \ll \omega_0$. The parameter $r_{13}(\mathbf{r}_\perp)$ takes the value r_{13} for $\mathbf{r}_\perp$ within the AlN and 0 elsewhere. We also assume that $\frac{\partial B_i(s)}{\partial s} = 0$ when the microwave field is absent, meaning that

$$\left(\nabla_\perp + \frac{\omega_i^2 \epsilon_r(\mathbf{r}_\perp, \omega_i)}{c^2} \right) f(\mathbf{r}_\perp) B_i(s) e^{-j\kappa_i s - \alpha s} = (\kappa_i - j\alpha)^2 f(\mathbf{r}_\perp) B_i(s) e^{-j\kappa_i s - \alpha s} \tag{3.10}$$

If we further assume that the modulation is weak such that $|B_\pm| \ll |B_0|$ and that the attenuation is low such that $\alpha \ll \kappa_i$ we obtain the following set of differential equations:

$$f(\mathbf{r}_\perp) \frac{\partial B_0(s)}{\partial s} = 0 \tag{3.11}$$

$$f(\mathbf{r}_\perp) \frac{\partial B_+(s)}{\partial s} = r_{13}(\mathbf{r}_\perp) f(\mathbf{r}_\perp) \frac{\omega_0 n_0^4}{4c n_{\text{eff}}(\omega_0)} B_0(0) A_\Omega(s) e^{j\Delta\kappa s} \tag{3.12}$$

$$f(\mathbf{r}_\perp) \frac{\partial B_-(s)}{\partial s} = -r_{13}(\mathbf{r}_\perp) f(\mathbf{r}_\perp) \frac{\omega_0 n_0^4}{4c n_{\text{eff}}(\omega_0)} B_0(0) A_\Omega^*(s) e^{-j\Delta\kappa s} \tag{3.13}$$

where we have assumed that, because $\Omega \ll \omega_0$, we have $\omega_+ / n_{\text{eff}}(\omega_+) \approx \omega_- / n_{\text{eff}}(\omega_-) \approx$

$\omega_0/n_{\text{eff}}(\omega_0)$. Here $\Delta\kappa \equiv \kappa_+ - \kappa_0 = \kappa_0 - \kappa_-$ is described as follows:

$$\Delta\kappa = \frac{\Omega n_g}{c} \tag{3.14}$$

$$n_g = n_{\text{eff}}(\omega_0) + \omega_0 \frac{\partial n_{\text{eff}}}{\partial \omega} \tag{3.15}$$

Multiplying both sides of equations 3.11-3.13 by $f^*(\mathbf{r}_\perp)$ and integrating over the plane perpendicular to s we obtain

$$\frac{\partial B_0(s)}{\partial s} = 0 \tag{3.16}$$

$$\frac{\partial B_+(s)}{\partial s} = \left(\int_{\text{AlN}} |f(\mathbf{r}_\perp)|^2 dA\right) \frac{\omega_0 n_0^4 r_{13}}{4c n_{\text{eff}}(\omega_0)} B_0(0) A_\Omega(s) e^{j\Delta\kappa s} \tag{3.17}$$

$$\frac{\partial B_-(s)}{\partial s} = -\left(\int_{\text{AlN}} |f(\mathbf{r}_\perp)|^2 dA\right) \frac{\omega_0 n_0^4 r_{13}}{4c n_{\text{eff}}(\omega_0)} (\mathbf{r}_\perp) B_0(0) A_\Omega^*(s) e^{-j\Delta\kappa s} \tag{3.18}$$

where the integral $\left(\int_{\text{AlN}} |f(\mathbf{r}_\perp)|^2 dA\right)$ is taken over $r_\perp$ within the AlN core and represents the fraction of the optical power confined to the core. We may then integrate to find $B_\pm(L)$ in terms of $B_0(0)$ and $A_\Omega(s)$:

$$B_+(L) = B_+(0) + \frac{\omega_0 n_0^4}{4c n_{\text{eff}}(\omega_0)} r_{13} B_0(0) \int_0^L A_\Omega(s) e^{j\Delta\kappa s} ds \tag{3.19}$$

$$B_-(L) = B_-(0) - \frac{\omega_0 n_0^4}{4c n_{\text{eff}}(\omega_0)} r_{13} B_0(0) \int_0^L A_\Omega^*(s) e^{-j\Delta\kappa s} ds \tag{3.20}$$

Let us define the following quantities:

$$\zeta e^{j\theta_\zeta} \equiv \int_0^L A_\Omega(s) e^{j\Delta\kappa s} ds \tag{3.21}$$

$$m \equiv \frac{\omega_0 n_0^4 \zeta}{2cn_{\text{eff}}(\omega_0)} r_{13} \tag{3.22}$$

where ζ and θ_ζ are real. Then

$$B_+(L) = B_+(0) + \frac{m}{2} e^{j\theta_\zeta} B_0(0) \tag{3.23}$$

$$B_-(L) = B_-(0) - \frac{m}{2} e^{-j\theta_\zeta} B_0(0) \tag{3.24}$$

Utilizing equation 3.5 can now solve for the amplitudes of output field E_C in terms of the input field amplitude A_0:

$$C_0 = \frac{(\sqrt{R} - ae^{-j\theta_0})A_0}{1 - \sqrt{R}ae^{-j\theta_0}} \tag{3.25}$$

$$C_\pm = \frac{\mp maTA_0 e^{\pm j\theta_\zeta} e^{-j\theta_\pm}}{2(1 - \sqrt{R}ae^{-j\theta_0})(1 - \sqrt{R}ae^{-j\theta_\pm})} \tag{3.26}$$

where $a = e^{-\alpha L}$, and $\theta_{0,\pm} = \kappa_{0,\pm} L = n_{\text{eff}}(\omega_{0,\pm})\omega_{0,\pm} L/c$. Here we see that C_0 behaves like we'd expect for a standard ring resonator, and the carrier power is minimized under the resonance condition that $\theta_0 = 2\pi N$ where N is an integer indicating the number of optical wavelengths that fit around the ring perimeter for a given resonant frequency. In the experiments described later in this chapter, L is on the order of 1 cm with $n_{\text{eff}} \approx 1.7$, and the vacuum optical wavelength of our laser source is around 1.55 μm. This leads to a value of N on the order of 10^4. In the case that $\sqrt{R} = a$, the transmitted carrier power drops completely to 0 on resonance, which we refer to

as critical coupling. To obtain an expression for the ring FSR we consider the spacing between neighboring resonances of C_0 at optical frequencies f_0 and f_1:

$$\frac{2\pi f_1 n_{\text{eff}}(\omega_1)L}{c} - \frac{2\pi f_0 n_{\text{eff}}(\omega_0)L}{c} = 2\pi \tag{3.27}$$

$$f_1 - f_0 = \Delta f = \frac{c}{n_g L} \tag{3.28}$$

where Δf is the ring FSR.

Maximizing each of $|C_\pm|$ with respect to $\theta_\pm$ yields $\theta_\pm = 2\pi N_\pm$ where $N_\pm$ are integers. Further maximizing the sideband powers with respect to θ_0 under this condition yields that $\theta_0 = 2\pi M$ for some integer M. These two conditions, along with the condition that $\theta_\pm = \theta_0 \pm \frac{2\pi n_g L}{\lambda_\Omega}$ implies that we can simultaneously achieve maxima of $|C_\pm|$ by tuning the carrier ω_0 to a resonance of the ring resonator ($\theta_0 = 2\pi M$), and designing the ring resonator such that $\frac{\Omega n_g L}{c} = 2\pi$, ensuring that $\theta_\pm = 2\pi N_\pm$ with $N_\pm = M \pm 1$. Therefore, to maximize $|C_\pm|$ we tune the optical carrier (ω_0) to resonance and design our ring such that $\frac{\Omega}{2\pi} = f_\Omega = \frac{c}{n_g L}$, meaning the ring FSR matches the microwave frequency of interest. Taking these conditions and evaluating equation 3.21 we see that if $A_\Omega(s) = A_\Omega$ is uniform in s, $\zeta = 0$ as $\Delta\kappa L = 2\pi$. For example, if the DRA near field has the same magnitude and direction at all points over the ring at any given instant in time, the net modulation integrates to 0 as light propagates around the ring. This is because by designing the ring FSR to match the microwave frequency of interest we have ensured that the round trip time of light in the ring matches the microwave period. As a result, for half of the propagation time the microwave field would point one way, while it would be equal and opposite for the remaining propagation time, leading to zero-sum modulation. If instead $A_\Omega(s) = A_\Omega$ over some length of the ring L_{eff} and 0 elsewhere, equation 3.22 is similar to the modulation depth δ

found in [52], and is maximized for $L_{\text{eff}} = \frac{L}{2}$. In the case where $A_\Omega(s) = A_\Omega$ for $0 < s < \frac{L}{2}$ and $A_\Omega(s) = -A_\Omega$ for $\frac{L}{2} < s < L$ where A_Ω is constant, m is doubled compared to the previous case. This motivates us to search for DRA modes that switch field polarity halfway around the ring. If we further consider the case that the ring is critically coupled such that $\sqrt{R} = a$ and the optical and microwave frequencies are tuned to maximize $|C_\pm|$ we obtain

$$|C_\pm| = \frac{maA_0}{2(1-a^2)} \tag{3.29}$$

Using the equation for finesse $\mathcal{F}$ as a function of a from [47], we obtain

$$|C_\pm| = \frac{m\mathcal{F}A_0}{2\pi} \tag{3.30}$$

and we can see that the sideband amplitudes are enhanced from the case of single pass modulation by a factor of $\mathcal{F}/\pi$.

3.2.2 DRA design and simulation

To engineer the DRA size and shape, COMSOL finite element method (FEM) eigenmode solver is used to find the resonant modes of the DRA, which is a proprietary ceramic (Exxelia 5080) with a relative permittivity of $\epsilon_r = 78$ and a dielectric loss tangent of 0.000625 at 5 GHz. This loss tangent is included in the COMSOL simulations and is assumed to be linear with respect to frequency. Keeping in mind the spatial requirement that the resonant field of the DRA should switch polarity halfway around the ring, we design a DRA structure that is a half cylinder with radius of 1mm and length of 4mm. The high value of ϵ_r allows for a high near-field

enhancement when the DRA is resonantly excited while simultaneously reducing the required DRA size for a given resonant frequency of interest. The dimensions of the DRA modify the resonant frequency, and are chosen to obtain a simulated resonant frequency of approximately 14 GHz. In order to excite a mode in which the field switches polarity, a ground plane is introduced in close proximity to the large flat side of the DRA. Simulation shows that the strength of the electric field between this ground plane and the DRA flat is increased as the distance between the two decreases. This is important, as the AlN ring resonator is designed to lie between these two surfaces. In order to minimize this distance and thus maximize the field in the AlN, degenerately doped silicon is simultaneously used as the substrate for the AlN ring resonator as well as the ground plane for the DRA. Once a suitable DRA mode is found, COMSOL RF solver is then used to simulate the response of the DRA to an incident x-polarized plane wave propagating in the $-z$ direction with E-field $E_{in} = 1$ V/m as a function of frequency near the DRA resonance. Figure 3.4a shows a schematic diagram of the device indicating the polarization and propagation direction of the incident microwave radiation used in these simulations. Figure 3.4b shows a cross section through the center of the DRA, with the simulated normalized z component of the electric displacement field $D_z = \epsilon E_z$ superposed when the DRA is excited by a plane wave on resonance. The red arrows indicate the direction of the overall displacement field $\mathbf{D}$. The proposed locations of the AlN waveguides are also indicated in figure 3.4b, but the waveguides themselves are too small to be included in the simulation. To evaluate the z-directed field enhancement of the DRA, we take the maximum z-directed E-field E_z along a line below the DRA center and parallel to the x axis that lies in the plane containing the AlN waveguides. We then divide this maximum E_z by the incident plane wave E-field of $E_{in} = 1$ V/m to find the z-directed field enhancement factor, which is then evaluated as a function of frequency. The results can be seen in Figure 3.4c

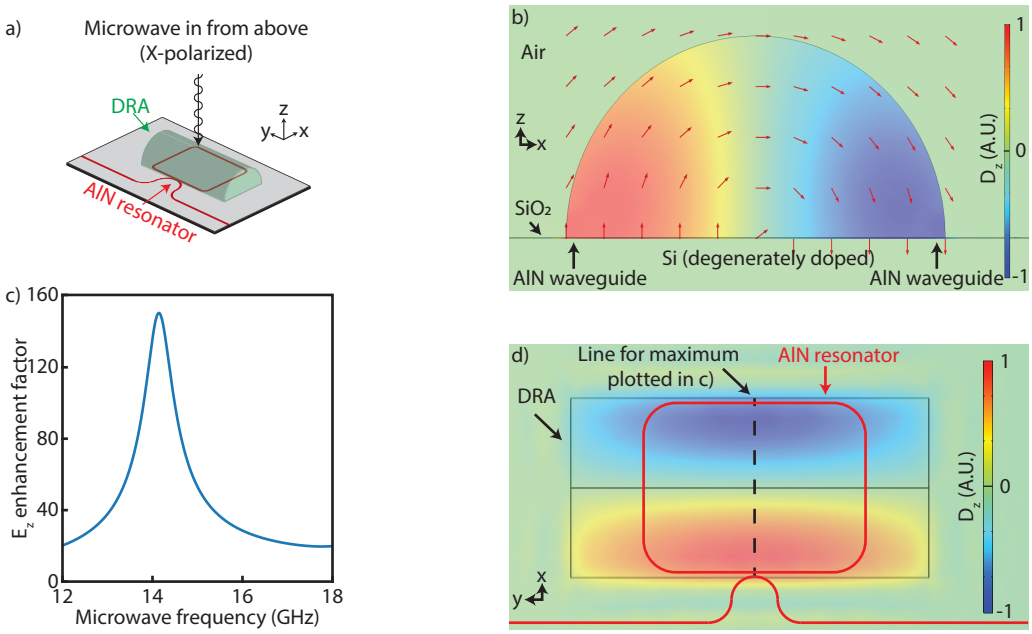

Figure 3.4: a) Schematic diagram of the doubly-resonant device indicating the polarization and propagation direction of the incident microwave radiation used in simulation. b) Cross section through the center of the DRA, with the normalized z component of the electric displacement field $D_z = \epsilon E_z$ superposed when the DRA is excited on resonance by an x-polarized plane wave propagating in the $-z$ direction as shown in a). The red arrows indicate the direction of the overall displacement field $\mathbf{D}$. c) z-directed field enhancement factor vs. frequency d) Top down of the DRA with the normalized z component of the electric displacement field $D_z = \epsilon E_z$ at the plane containing the AlN resonator superposed when the DRA is excited on resonance by an x-polarized plane wave propagating in the $-z$ direction. Also superposed is the line from which the maximum was taken in c), and a schematic drawing of the AlN resonator location showing the switch in polarity as light propagates along the ring.

showing a maximum enhancement of approximately 150 corresponding to the DRA resonance. Figure 3.4d shows a top down view of the DRA, superposed with the z-directed displacement field in a plane below the DRA which contains the AlN resonator. A schematic of the AlN resonator is also superposed along with a dashed line corresponding to the line used to calculate the z-directed field enhancement factor. We now see the effect of the DRA is twofold: not only does the DRA provide an enhancement in microwave field, but it also changes the direction of the microwave field to point in the z direction at the location of the AlN, aligning it with the AlN crystal axis. The switch in polarity across the center of the DRA can clearly be seen in

figure 3.4b. Due to the ground plane, this resonant mode is similar to the $TE_{01\delta}$ mode of a full dielectric cylinder. This mode is polarization sensitive and will not be excited by a y-polarized wave. The resonant frequency of this DRA mode depends primarily on the DRA radius and ϵ_r, and is only slightly changed by modifying the DRA length. This allows us to increase the DRA length to ensure the entire AlN ring is covered by the DRA without significantly changing the DRA frequency.

3.2.3 AlN ring design and fabrication

In order to match the ring FSR to the DRA resonant frequency, the group index of the waveguide structure must be calculated from simulation. The waveguides are designed to be 400 nm thick and have a width of approximately 1.25 μm, and are designed for TE mode operation. In this design A 2.9 μm SiO_2 buffer layer below the AlN isolates the waveguide from the conductive losses in the degenerately doped Si substrate, and a 3 μm thick SiO_2 top cladding protects the waveguide from damage. Our fabrication process has shown that the finished waveguides have a base that is wider than the design, and sidewalls that are at a 75 degree angle from the substrate. The simulation of the waveguide structure takes the widened base and sloped sidewalls into account. Figure 3.5a shows a schematic diagram of the waveguide structure, while figure 3.5b shows the electric field magnitude for the TE waveguide mode as a function of position as simulated with Ansys Lumerical MODE finite difference eigenmode solver. This simulation also yields a group index for the structure of around 2.1. Figure 3.5c shows a scanning electron micrograph of the fabricated polished waveguide facet.

The directional coupler that connects the AlN ring to the input bus waveguide consists of

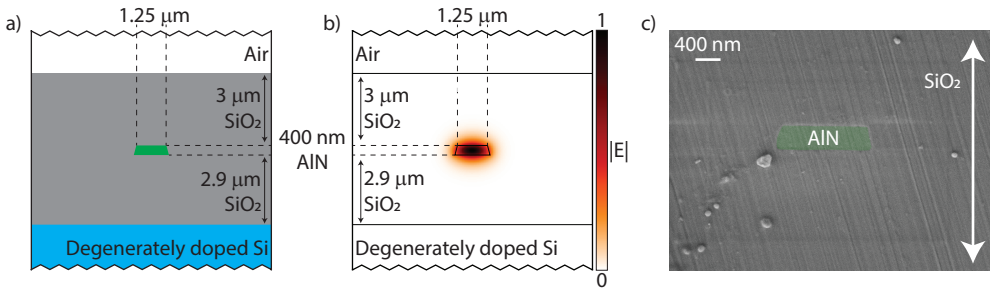

Figure 3.5: a) Schematic diagram showing the AlN waveguide structure. b) AlN waveguide structure with TE mode electric field magnitude superposed as simulated in Ansys Lumerical MODE finite difference eigenmode solver. c) Scanning electron micrograph of the polished waveguide end facet.

two parallel waveguides with a center-to-center spacing of 2 μm. With this spacing and bend radius of 250 μm, we find the contribution to the coupler from the curved waveguide sections leading up to the parallel waveguides to be negligible. Therefore the fraction of power coupled into the ring is approximated as

$$T = \sin^2\left(\frac{\pi \delta n L}{\lambda}\right) \tag{3.31}$$

where δn is the difference in effective index between the symmetric and anti-symmetric modes of the coupled waveguide structure, λ is the wavelength of operation and L is the length of the coupler. Ansys Lumerical MODE simulation of the coupled structure yields $\delta n = 0.003$. This allows us to design the coupler for critical coupling once the waveguide propagation loss is known.

Figure 3.6 shows a step-by-step schematic of the AlN device fabrication process. Fabrication of the AlN structures begins with degenerately doped, single side polished silicon substrates on which a 2.9 μm thick wet thermal SiO_2 buffer layer is grown. The oxidized substrates are then sent to Carnegie Mellon University where a 400 nm thick AlN film is sputter deposited. This

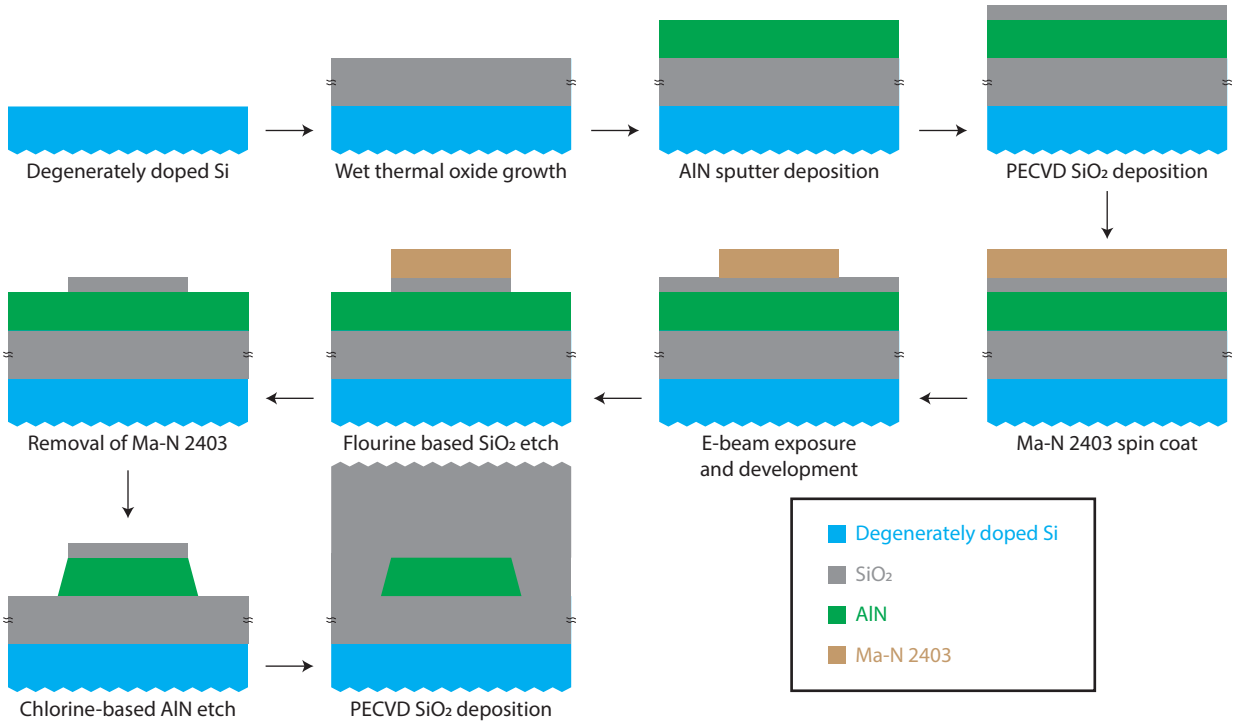

Figure 3.6: Step-by-step schematic of the AlN waveguide fabrication process.

film is poly-crystalline, but the crystal grains are all oriented such that the crystal axis of AlN is directed normal to the Si substrate. Having a c-axis aligned film is important for the device design, as the electro-optic effect in AlN is axis dependent and strongest when the microwave field is polarized parallel to the crystal axis. Once the substrates have been returned, a 2 cm x 2 cm chip is cleaved from the substrate and a 150 nm thick SiO_2 hard mask is deposited on the chip via plasma enhanced chemical vapor deposition (PECVD). Next, Ma-N 2403 negative-tone electron beam resist is spun atop the chip and patterned in an Elionix 100 kV electron beam lithography tool. After development, the patterned resist acts as a mask to pattern the 150 nm SiO_2 layer, which is etched in a flourine-based inductively coupled plasma reactive ion etch (ICPRIE), performed in an Oxford PlasmaPro 100 Cobra ICP tool. The remaining resist is then removed in acetone and the patterned SiO_2 is used as a mask to pattern the AlN via chlorine-based ICPRIE in a second Oxford PlasmaPro 100 Cobra ICP tool using the following recipe: 20 sccm Cl2, 10

sccm BCl3, 2 mTorr chamber pressure, 20 C table temperature, 300 W ICP power, 300 W high frequency (HF) power, 0 Torr backside helium pressure. In order to obtain low-loss waveguide propagation, it is critical that the AlN etch step provide smooth vertical waveguide side walls. The high HF power used in this recipe improves the directionality of the etch, producing smooth waveguide walls at approximately a 75 degree angle to the chip surface. During the etch, the chip rests in a recessed pocket on a Si carrier wafer. No adhesive is used between the chip and the carrier in order to avoid contamination during the etch. After etching, a SiO_2 cladding layer is deposited via PECVD to protect the AlN structures. While the target thickness for the cladding used in simulation is 3 μm, spectral reflectance measurements of the deposited cladding indicate an actual thickness of 2.8 μm. Finally, the edges of the chip are diced and polished to allow for coupling of light into the facets of the AlN waveguides.

3.2.4 Experiment and results

Figure 3.7a shows a schematic of the experimental setup. Emission from a tunable laser

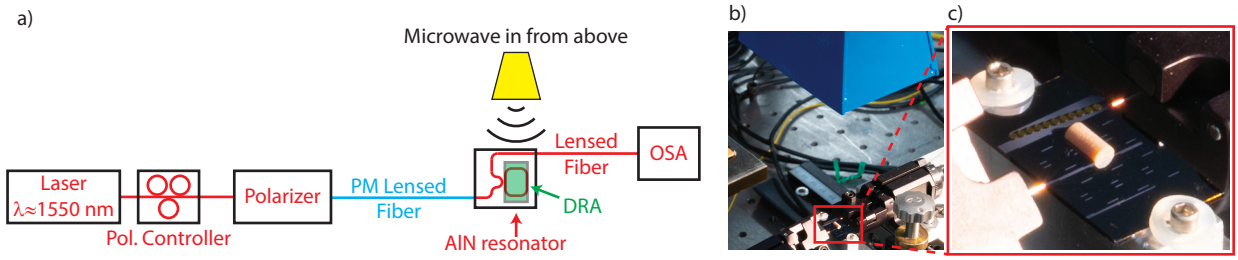

Figure 3.7: a) Schematic of the measurement setup. PM: polarization maintaining, OSA: optical spectrum analyzer. b) Photograph of the measurement setup showing the chip, DRA, and horn antenna. c) Close up photograph of the chip and DRA.

with a wavelength near 1550 nm is edge-coupled to the AlN waveguides via a polarization-maintaining (PM) lensed fiber in close proximity to the polished chip facet which is aligned using 3-axis piezoelectric stages. A polarization controller and polarizer prior to the PM lensed fiber

ensure that the laser light polarization is aligned with one of the axes of the fiber, and a rotating fiber mount ensures the polarization at the output of the fiber is aligned with the TE mode of the AlN waveguides. The output of the optical resonator on-chip is coupled into a second lensed fiber and the output is detected by an optical spectrum analyzer (OSA). The DRA is manually placed on top of the AlN ring using a microscope and patterned alignment marks for guidance, and a horn antenna is suspended approximately 7 cm above the chip and is oriented such that the emitted radiation is polarized to excite the DRA mode (x-polarized). Figure 3.7b shows a photograph of the measurement setup, and figure 3.7c shows a close-up of the fiber-coupled chip with the DRA resting on top.

In order to verify the electro-optic effect in AlN, smaller ring resonators with an FSR of approximately 87 GHz were fabricated, and gold electrodes were patterned above each of the rings via aligned photo-lithography and metal film liftoff. These electrodes can be seen above the DRA in figure 3.7c. An electrical probe is then used to contact each electrode and apply a voltage between the electrode and the Si substrate. The thermal oxide on the back of the chip was removed via ICPRIE and a layer of gold was deposited to ensure good electrical contact to the Si. Figure 3.8a shows a schematic of the device layers with the electrode sandwich structure. Applying a DC voltage to the electrode causes the effective index of the ring resonator to change which in turn causes the resonant wavelength λ_0 to shift. Figure 3.8c shows the normalized optical transmission as a function of wavelength for applied voltages from -20 to 20 Volts. Figure 3.8d shows a linear fit of the resonant wavelength λ_0 as a function of applied voltage. From the slope of this fit we can extract the material electro-optic coefficient r_{13}. To do this we need to know two additional parameters. The first necessary parameter is the ratio of voltage applied to the z-directed electric field E_z in the AlN, which is a function of the distance between the

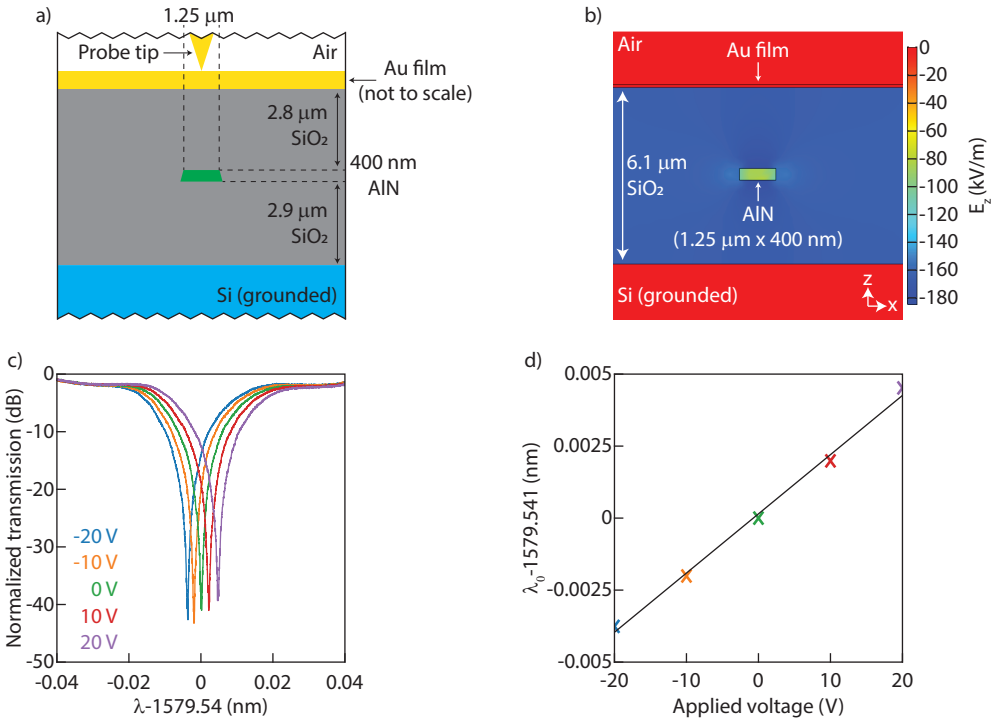

Figure 3.8: a) Schematic of the device layers showing the electrode sandwich structure. b) COMSOL electrostatics simulation of the sandwich structure showing the z-directed electric field E_z when 1V is applied to the electrode. c) Normalized transmisson as a function of wavelength for applied voltages from -20 V to 20 V. d) Plot of the resonant wavelength λ_0 as a function of applied voltage with linear fit superposed.

electrode and Si ground plane as well as the refractive index contrast between the AlN and SiO_2. The distance between the electrode and Si ground plane is the sum of the film thicknesses of the SiO_2 buffer layer (2.9 μm), AlN layer (400 nm), and SiO_2 cladding layer (2.8 μm), totalling 6.1 μm. An electrostatic COMSOL simulation of the device structure is shown in figure 3.8b. This simulation shows the z-directed electric field $E_z \approx -85$ kV/m at the center of the AlN waveguide when one volt is applied to the electrode. For simplicity, we will assume this field is uniform across the AlN waveguide. The second necessary parameter is the ratio of waveguide effective index change to AlN index change $\frac{\Delta n_{\text{eff}}}{\Delta n_0}$. From simulations of the waveguide mode shown in figure 3.5b, we can see that the mode is not entirely confined within the AlN core. Therefore we expect $\frac{\Delta n_{\text{eff}}}{\Delta n_0}$ to be less than one. Using Ansys Lumerical MODE to fit Δn_{eff} vs.

Δn_0, we obtain $\frac{\Delta n_{\text{eff}}}{\Delta n_0} = 0.83$. Finally, we have the following equation for r_{13}

$$r_{13} = \frac{2n_g}{n_0^3 \lambda_0(0)} \left(\frac{E_z}{V}\right)^{-1} \left(\frac{\Delta n_{\text{eff}}}{\Delta n_0}\right)^{-1} \frac{\Delta \lambda_0}{\Delta V} \tag{3.32}$$

where $\lambda_0(0)$ is the resonant wavelength at 0 volts. Using this equation, the fit in figure 3.8c yields $r_{13} = 0.9$ pm/V. This agrees well with the result found in [56].

In order to verify the DRA frequency, a reflection measurement is set up as shown in figure 3.9a. Here the horn antenna is replaced by a hollow WR-62 microwave waveguide that is brought down atop the DRA sitting on the fabricated AlN chip. A vector network analyzer (VNA) is used to measure the fraction of power reflected back to the WR-62 waveguide. Simulations in Ansys HFSS indicate that a sharp decrease in reflected power should occur when the DRA is resonantly excited. Figure 3.9b shows the results of the reflection measurement in comparison to

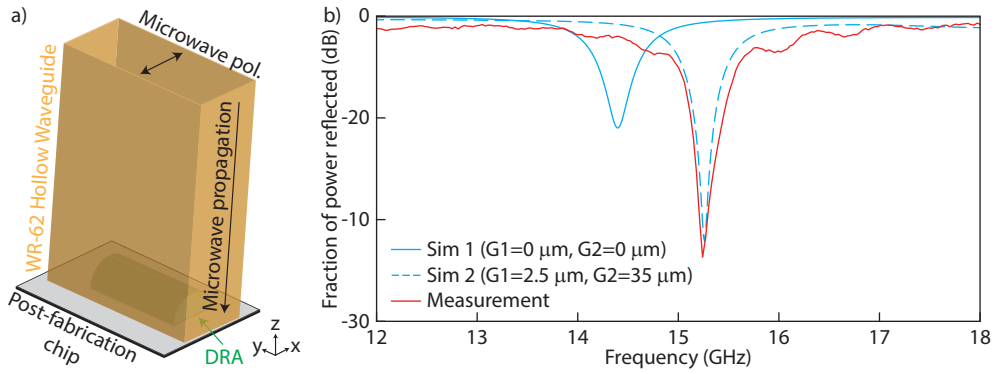

Figure 3.9: a) Measurement setup for DRA resonant frequency. A hollow WR-62 microwave waveguide is placed top down over the DRA and capped by the doped silicon substrate. Reflected power is measured with a vector network analyzer as a function of frequency. b) Measurement results as compared to the ideal simulation, and a simulation including a gap between the DRA and substrate (G1), as well as a gap between the WR-62 waveguide and substrate (G2). Simulations done in Ansys HFSS.

two simulations. In the ideal simulation both the WR-62 waveguide and the DRA sit flush against the chip surface. In practice there is roughness in the DRA and chip surfaces which causes

separation and affects the resonant frequency of the DRA. In the simulation this is accounted for by adding a gap of air between the DRA and the chip surface (G1). Additionally, during the measurement the WR-62 waveguide is suspended from a z-axis stage and lowered until it is nearly touching the chip. The resulting gap between the WR-62 and the chip surface affects the depth of the DRA resonance and is accounted for in the simulation as a gap of air in the simulation between the WR-62 waveguide and the chip surface (G2). With reasonable values (G1=2.5 μm, G2=35 μm) the simulation and measurement agree closely showing a resonant frequency of approximately 15.2 GHz.

Next we characterize the AlN ring performance in the absence of microwave excitation. Figure 3.10a shows the optical transmission as a function of wavelength in the case where no microwave radiation is present and the upper axis shows the frequency detuning from center frequency f_0. The spectrum has a measured FSR of approximately 15.2 GHz and fitting each

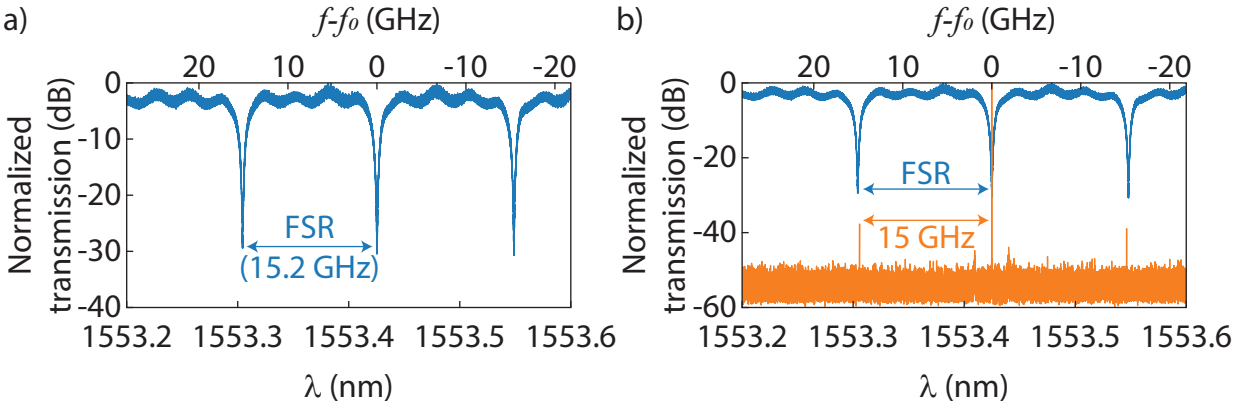

Figure 3.10: a) Normalized transmission vs. wavelength showing an extinction ratio of nearly 30 dB and an FSR of 15.2 GHz. Upper axis shows frequency detuning from center frequency f_0. b) Normalized transmission vs. wavelength with normalized modulated spectral measurement superposed. The modulated spectrum shows sidebands at 15 GHz spacing from the carrier.

of the resonances to a Lorentzian yields a loaded quality factor of about 1.1×10^5, indicating a propagation loss of around 1.74 dB/cm. The extinction ratio of the ring is nearly 30 dB, indicating

the ring is nearly critically coupled. Next, the laser is tuned to frequency f_0 and x-polarized microwave radiation at 15 GHz is used to excite the device. Figure 3.10b shows the normalized output spectrum of the modulated resonant tone superposed over the transmission spectrum in figure 3.10a. Modulation sidebands can be seen 15 GHz to either side of the carrier, and they line up well with the nearby resonances of the AlN ring. When the microwave polarization is rotated 90 degrees, the sidebands vanish below the noise floor, indicating the DRA resonance is no longer excited.

Next, we examine the dependence of the power in the modulation sidebands as a function of input microwave power, input microwave frequency, and input optical wavelength. Figure 3.11a shows the optical power in the right and left sidebands as a function of microwave power at the input of the horn antenna. From here out we refer to the sideband with higher wavelength as the right sideband. The solid lines in figure 3.11a have a slope of 1 and their y-intercepts are fit to the data. These lines show that the output power in the sidebands is nearly linear with respect to input power. Figure 3.11b shows the normalized power in the optical sidebands as a function of microwave frequency for a fixed input microwave power of 17.5 dBm when the optical carrier is tuned to resonance. In order to decouple the response of the device from the input optical power, the output sideband powers are normalized to the transmitted optical carrier power off resonance. Figure 3.11b shows a distinct peak when the microwave frequency is 15 GHz. A much weaker secondary peak can be seen at 16 GHz, and is attributed to a nearby resonant mode of the DRA. Figure 3.11c shows the normalized power in the sidebands as a function of laser detuning from resonance when the microwave power is fixed at 17.5 dBm and the microwave frequency is fixed at 15 GHz. The power is normalized in the same way as in figure 3.11b. A maximum can be seen in each sideband when the detuning is near 0. The slight separation in the sideband maxima with

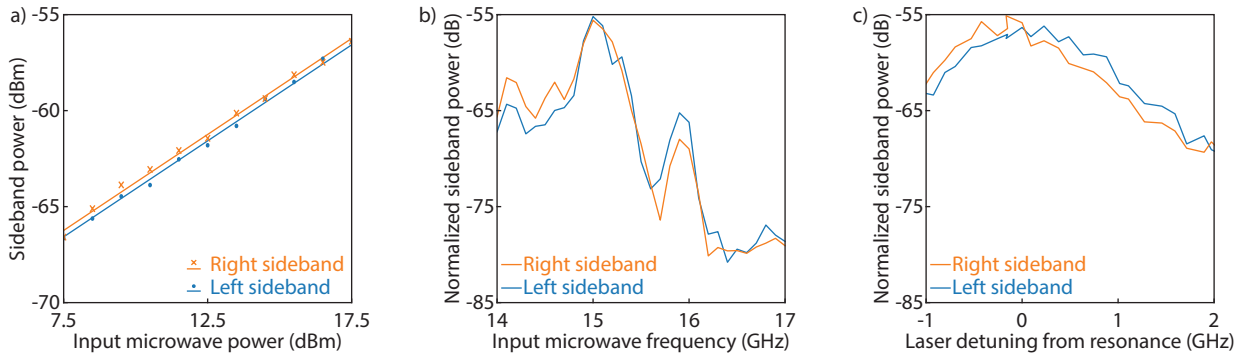

Figure 3.11: a) Power in optical sidebands as a function of power into the horn antenna when the microwave frequency is fixed at 15.1 GHz and the optical wavelength is tuned to resonance. The solid lines have slope 1 and their y-intercepts are fit to the data. b) Normalized power in optical sidebands as a function of microwave frequency for an input microwave power of 17.5 dBm when the optical carrier is resonant. Power is normalized by the carrier power off resonance. c) Normalized power in optical sidebands as a function of optical detuning for an input microwave power of 17.5 dBm and microwave frequency fixed at 15 GHz. Power is normalized by the carrier power off resonance.

respect to detuning is a result of the slight mismatch of 200 MHz between the optical FSR and DRA resonant frequency.

To illustrate the importance of matching the DRA resonant frequency to the ring FSR, the measurements from figure 3.11c and d were repeated with a ring resonator that has a higher FSR of approximately 16 GHz. Figure 3.12a and b show the normalized sideband power vs microwave frequency for the 15.2 GHz FSR and 16 GHz FSR rings respectively. A peak can be seen at 15 GHz in both cases, but the overall carrier-normalized power is lower in the 16 GHz FSR case. Figure 3.12c and d show the normalized sideband power vs optical detuning for the 15.2 GHz FSR and 16 GHz FSR rings respectively. Here a greater mismatch between the maxima in the left and right sidebands can be seen in the 16 GHz FSR case, as well as a slight decrease in the maximum values themselves. In both cases the sideband powers are approximately equal when the optical carrier is tuned to resonance.

As a figure of merit for the performance of the device, we can extrapolate the data from

figure 3.11a to determine the minimum detectable microwave intensity. If we consider the OSA noise floor of approximately -79 dBm to be the minimum detectable sideband power, this yields a minimum detectable input power to the horn antenna of approximately -5 dBm. Assuming a gaussian beam approximation for the beam radiated by the horn yields the following equation for the on-axis intensity at a distance r from the horn input:

$$I(z) = \frac{P_{in}}{\frac{G\lambda_{\Omega}}{16\pi} + \frac{4\pi r^2}{G}} \tag{3.33}$$

where $G = 100$ is the horn antenna gain (20 dBi) and $P_{in} = 0.32$ mW (-5 dBm) is the power in to the horn. Here we measure the distance $r = 21$ cm from the horn input rather than the aperture, as the beam begins to diverge immediately after entering the horn. Plugging in values for P_{in}, r, and G, this yields a minimum detectable intensity of approximately 7 mW/m^2 which is similar to the minimum detectable intensity reported for other antenna-coupled integrated photonic modulators [65].

3.2.5 Conclusions

Here I have demonstrated the design, fabrication, and performance of an entirely metal-free doubly-resonant microwave photonic receiver in AlN. The electro-optic coefficient r_{13} in the AlN sputtered thin film was measured to be approximately 0.9 pm/V and is in good agreement with values reported elsewhere. The device shows a strong response when simultaneously excited by both a resonant optical carrier and resonant microwave radiation, characterized by a minimum detectable microwave intensity of 7 mW/m^2. In the future, exploration of different DRA structures has the potential to modify the device performance. For example, making use of a disk-shaped

DRA could allow for a receiver that is insensitive to the in-plane direction of linearly polarized microwave radiation. A means of affixing the DRA to the substrate without affecting the resonant frequency is also of future interest, although the dependence of the resonant frequency on the intimacy of the interface between the DRA and the chip surface poses a challenge.

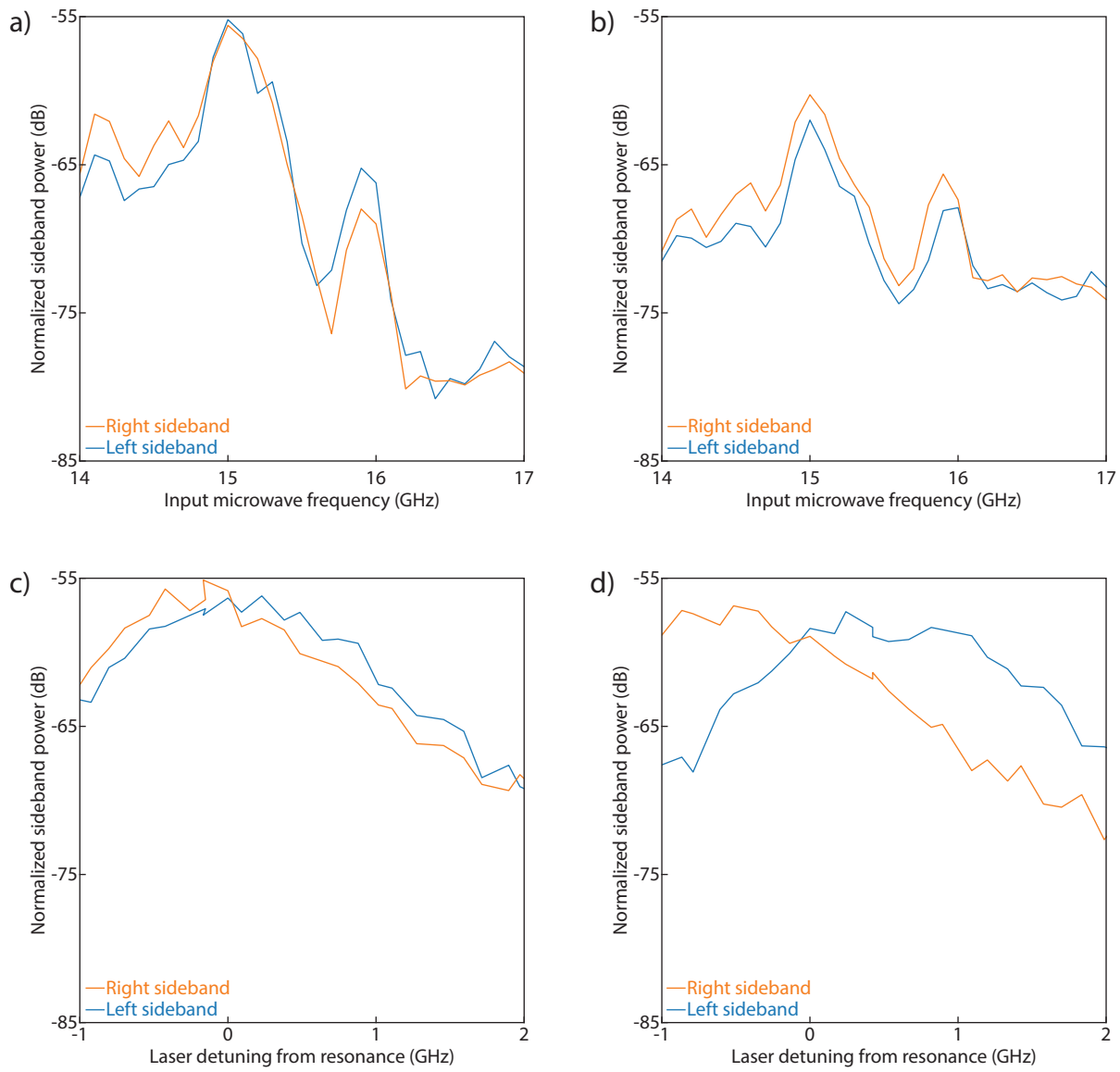

Figure 3.12: a) Normalized power in optical sidebands as a function of microwave frequency for the 15.2 GHz FSR ring. b) Normalized power in optical sidebands as a function of microwave frequency for the 16 GHz FSR ring. In both a) and b) the input microwave power is 17.5 dBm and the optical carrier is resonant. c) Normalized power in optical sidebands as a function of optical detuning for the 15.2 GHz FSR ring. d) Normalized power in optical sidebands as a function of optical detuning for the 16 GHz FSR ring. In both c) and d) the input microwave power is 17.5 dBm and the microwave frequency is fixed at 15 GHz. In a) b) c), and d) the sideband power is normalized by the carrier power off resonance.

Chapter 4: Conclusions and outlook

In this thesis I have described microwave electro-optic receiver experiments at both the system and device level. Microwave photonic systems and devices are especially interesting for applications that can benefit greatly from their reduced size and weight and/or from low-loss fiber-optic transmission. Some examples include avionics sensing and radar applications [66,67], where multiple microwave signals need to be transmitted to a central location from several physically distant receivers. Additionally, MWP systems can have very high instantaneous bandwidths, and often boast tunability or reconfigurability that is difficult to achieve in traditional microwave systems [68].

At the system level I described an electro-optic down-converting I/Q mixer that takes a microwave input at frequency f_1 and mixes it with a local oscillator (LO) at frequency f_{LO} to produce in phase (I) and quadrature (Q) outputs at intermediate frequency (IF) $f_{\mathrm{IF}} = |f_1 - f_{\mathrm{LO}}|$. By combining these I an Q outputs in a 90 degree electrical hybrid, we can separate contributions to the IF from a signal above the LO $f_1 = f_{\mathrm{LO}} + f_{\mathrm{IF}}$ and its image below the LO $f_2 = f_{\mathrm{LO}} - f_{\mathrm{IF}}$ into different outputs, preventing them from interfering despite being down-converted to the same IF frequency. The system is designed using commercially available components and boasts reduced complexity compared to other designs, requiring only a single laser and modulator and, in principle, only one carefully controlled bias voltage. We demonstrated 40 dB of isolation

between the outputs and a 3dB bandwidth of approximately 20 GHz which is determined by the asymmetric Mach-Zehnder interferometer (AMZI) used. We also demonstrated the wideband functionality of the system by showing a 1 Gbaud quadrature phase-shift keyed (QPSK) pseudo-random bit sequence (PRBS11) can be down-converted and recovered at the output despite the presence of a strong interfering tone at its image frequency.

At the device level, I described the design, fabrication, and characterization of an entirely metal-free doubly-resonant microwave receiver in aluminum nitride (AlN). In the microwave regime, a dielectric resonator antenna (DRA) is used to concentrate incoming microwave radiation, as well as modify the direction of the microwave electric field in the vicinity of the AlN. In the optical regime, an on-chip AlN ring resonator is used to concentrate the optical carrier thereby increasing the effect of the microwave modulation. To maximize device performance, the free spectral range (FSR) of the AlN ring is carefully matched to the DRA microwave resonant frequency. When the device is simultaneously excited by resonant microwave radiation and a resonant optical carrier, a maximum microwave sensitivity of approximately 7 mW/m^2 is achieved.

In the future, integrating multiple system level components on chip is attractive due to the potential reduction in size and weight from combining several packaged components onto a single chip. For example, one could consider including a standard MZM in parallel with the doubly-resonant ring modulator described in chapter 3. By modulating this MZM with a local oscillator signal, one could achieve on-chip down-conversion similar to that described in chapter 2. While traditional bulk lithium niobate modulator structures make on-chip system integration difficult due to their relatively large size, new material platforms for on chip electro-optic modulation are being developed such as the thin film lithium niobate mentioned in chapter 1 or the aluminum

nitride modulators discussed in chapter 3. Barium titanate is also an attractive option, boasting electro-optic coefficients that are an order of magnitude larger than lithium niobate [69, 70]. Barium titanate also has the advantage of being able to be grown on silicon substrates via molecular beam epitaxy, although patterning and fabrication challenges still remain. Electro-optic polymer modulators have also been reported [71], although long-term polymer instability remains problematic.

Dielectric resonator antennas are becoming increasingly attractive options for high frequency, narrow bandwidth applications such as automotive radar [72]. DRA structures can be significantly smaller than their conducting counterparts due to their high relative permittivity, and they are also free from conductive losses that can play a significant role at high microwave frequencies. Several DRA based MWP receivers placed at different locations on a vehicle could easily take advantage of fiber-optic transmission to an on-board central processor as traditional coaxial transmission line losses become insurmountable at higher microwave frequencies. With respect to the work described in chapter 3, future exploration of different dielectric resonator antenna structures has the potential to yield advantages. For example, use of a disk shaped DRA has the potential to yield a device with a response that is independent of the in-plane linear polarization of incoming microwave radiation. Additionally, one could consider integrated fabrication of the DRA structure on-chip, although choice of a suitable material for integrated DRA fabrication is necessary. Polymer or polymer-ceramic mixture based DRA structures have been reported, using the photosensitive properties of the polymer to pattern the DRA structure [73, 74], and 3D printed DRA structures with tunable relative permittivity have been demonstrated using fused deposition modeling [75]. However, these structures have a relative permittivity that is much lower than the ceramic DRA described in this work. Fabrication of the ring resonator structures using

a material with a larger electro-optic coefficient than ALN has the potential to improve device performance, although this comes with significant complication of the fabrication process.

Bibliography

[1] Steven T. Lipkowitz, Timothy U. Horton, and Thomas E. Murphy. Wideband microwave electro-optic image rejection mixer. *Optics Letters*, 44(19):4710–4713, October 2019. Publisher: Optica Publishing Group.

[2] José Capmany and Dalma Novak. Microwave photonics combines two worlds. *Nature Photonics*, 1(6):319–330, June 2007. Number: 6 Publisher: Nature Publishing Group.

[3] E.L. Wooten, K.M. Kissa, A. Yi-Yan, E.J. Murphy, D.A. Lafaw, P.F. Hallemeier, D. Maack, D.V. Attanasio, D.J. Fritz, G.J. McBrien, and D.E. Bossi. A review of lithium niobate modulators for fiber-optic communications systems. *IEEE Journal of Selected Topics in Quantum Electronics*, 6(1):69–82, January 2000. Conference Name: IEEE Journal of Selected Topics in Quantum Electronics.

[4] R. V. Schmidt and I. P. Kaminow. Metal-diffused optical waveguides in LiNbO3. *Applied Physics Letters*, 25(8):458–460, October 1974. Publisher: American Institute of Physics.

[5] Andrew J. Mercante, Peng Yao, Shouyuan Shi, Garrett Schneider, Janusz Murakowski, and Dennis W. Prather. 110 GHz CMOS compatible thin film LiNbO3 modulator on silicon. *Optics Express*, 24(14):15590–15595, July 2016. Publisher: Optica Publishing Group.

[6] Cheng Wang, Mian Zhang, Xi Chen, Maxime Bertrand, Amirhassan Shams-Ansari, Sethumadhavan Chandrasekhar, Peter Winzer, and Marko Lončar. Integrated lithium niobate electro-optic modulators operating at CMOS-compatible voltages. *Nature*, 562(7725):101–104, October 2018. Number: 7725 Publisher: Nature Publishing Group.

[7] M. Levy, R. M. Osgood, R. Liu, L. E. Cross, G. S. Cargill, A. Kumar, and H. Bakhru. Fabrication of single-crystal lithium niobate films by crystal ion slicing. *Applied Physics Letters*, 73(16):2293–2295, October 1998. Publisher: American Institute of Physics.

[8] Payam Rabiei and Peter Gunter. Optical and electro-optical properties of submicrometer lithium niobate slab waveguides prepared by crystal ion slicing and wafer bonding. *Applied Physics Letters*, 85(20):4603–4605, November 2004. Publisher: American Institute of Physics.

[9] Andrew J. Mercante, David L. K. Eng, Matthew Konkol, Peng Yao, Shouyuan Shi, and Dennis W. Prather. Thin $LiNbO_3$ on insulator electro-optic modulator. *Optics Letters*, 41(5):867–869, March 2016. Publisher: Optica Publishing Group.

[10] Naoki Mitsugi, Hirotoshi Nagata, Kaori Shima, and Masumi Tamai. Challenges in electron cyclotron resonance plasma etching of LiNbO3 surface for fabrication of ridge optical waveguides. *Journal of Vacuum Science & Technology A*, 16(4):2245–2251, July 1998. Publisher: American Vacuum Society.

[11] K. Noguchi, O. Mitomi, K. Kawano, and M. Yanagibashi. Highly efficient 40-GHz bandwidth Ti:LiNbO/sub 3/ optical modulator employing ridge structure. *IEEE Photonics Technology Letters*, 5(1):52–54, January 1993. Conference Name: IEEE Photonics Technology Letters.

[12] Chi Xiong, Wolfram H. P. Pernice, and Hong X. Tang. Low-Loss, Silicon Integrated, Aluminum Nitride Photonic Circuits and Their Use for Electro-Optic Signal Processing. *Nano Letters*, 12(7):3562–3568, July 2012.

[13] Soutik Sur and V. Venkataraman. Observation of Electro-Optic Pockels Effect at the Amorphous $\mathrm{Ti}{\mathrm{O}}_{2}$ and Metal Interface. *Physical Review Applied*, 10(1):014020, July 2018. Publisher: American Physical Society.

[14] G.K. Gopalakrishnan, R.P. Moeller, M.M. Howerton, W.K. Burns, K.J. Williams, and R.D. Esman. A low-loss downconverting analog fiber-optic link. *IEEE Transactions on Microwave Theory and Techniques*, 43(9):2318–2323, September 1995. Conference Name: IEEE Transactions on Microwave Theory and Techniques.

[15] J.T. Gallo and J.K. Godshall. Comparison of series and parallel optical modulators for microwave down-conversion. *IEEE Photonics Technology Letters*, 10(11):1623–1625, November 1998. Conference Name: IEEE Photonics Technology Letters.

[16] G.K. Gopalakrishnan, W.K. Burns, and C.H. Bulmer. Microwave-optical mixing in LiNbO/sub 3/ modulators. *IEEE Transactions on Microwave Theory and Techniques*, 41(12):2383–2391, December 1993. Conference Name: IEEE Transactions on Microwave Theory and Techniques.

[17] Vincent R. Pagán and Thomas E. Murphy. Electro-optic millimeter-wave harmonic downconversion and vector demodulation using cascaded phase modulation and optical filtering. *Optics Letters*, 40(11):2481–2484, June 2015. Publisher: Optica Publishing Group.

[18] Chunjing Yin, Jianqiang Li, Liang Shu, Zhenming Yu, Feifei Yin, Yue Zhou, Yitang Dai, and Kun Xu. Broadband lower-IF RF receiver based on microwave photonic mixer and Kramers-Kronig detection. *Optics Express*, 26(20):26400–26410, October 2018. Publisher: Optica Publishing Group.

[19] Jianqiang Li, Jia Xiao, Xiaoxiong Song, Yue Zheng, Chunjing Yin, Qiang Lv, Yuting Fan, Feifei Yin, Yitang Dai, and Kun Xu. Full-band direct-conversion receiver with enhanced port isolation and I/Q phase balance using microwave photonic I/Q mixer (Invited Paper). *Chinese Optics Letters*, 15(1):010014, January 2017. Publisher: Chinese Optical Society.

[20] Zhenzhou Tang, Fangzhen Zhang, Dan Zhu, Xihua Zou, and Shilong Pan. A photonic frequency downconverter based on a single dual-drive Mach-Zehnder modulator. In *2013*

IEEE International Topical Meeting on Microwave Photonics (MWP), pages 150–153, October 2013.

[21] Charles Middleton, Scott Meredith, Robert Peach, and Richard DeSalvo. Photonic frequency conversion for wideband RF-to-IF down-conversion and digitization. In *2011 IEEE Avionics, Fiber- Optics and Photonics Technology Conference*, pages 115–116, October 2011.

[22] Ali Altaqui, Erwin H. W. Chan, and Robert A. Minasian. Microwave photonic mixer with high spurious-free dynamic range. *Applied Optics*, 53(17):3687–3695, June 2014. Publisher: Optica Publishing Group.

[23] Wei Li, Wen Hui Sun, Wen Ting Wang, Li Xian Wang, Jian Guo Liu, and Ning Hua Zhu. Photonic-assisted microwave phase shifter using a DMZM and an optical bandpass filter. *Optics Express*, 22(5):5522–5527, March 2014. Publisher: Optica Publishing Group.

[24] Tianwei Jiang, Ruihuan Wu, Song Yu, Dongsheng Wang, and Wanyi Gu. Microwave photonic phase-tunable mixer. *Optics Express*, 25(4):4519–4527, February 2017. Publisher: Optica Publishing Group.

[25] Yongsheng Gao, Aijun Wen, Zhaoyang Tu, Wu Zhang, and Lin Lin. Simultaneously photonic frequency downconversion, multichannel phase shifting, and IQ demodulation for wideband microwave signals. *Optics Letters*, 41(19):4484–4487, October 2016. Publisher: Optica Publishing Group.

[26] B. Razavi. Design considerations for direct-conversion receivers. *IEEE Transactions on Circuits and Systems II: Analog and Digital Signal Processing*, 44(6):428–435, June 1997. Conference Name: IEEE Transactions on Circuits and Systems II: Analog and Digital Signal Processing.

[27] Dan Zhu and Shilong Pan. Photonics-Based Microwave Image-Reject Mixer. *Photonics*, 5(2):6, June 2018. Number: 2 Publisher: Multidisciplinary Digital Publishing Institute.

[28] J. Zhang, E. H. W. Chan, X. Wang, X. Feng, and B. Guan. High Conversion Efficiency Photonic Microwave Mixer With Image Rejection Capability. *IEEE Photonics Journal*, 8(4):1–11, August 2016. Conference Name: IEEE Photonics Journal.

[29] Lu Chao, Chen Wenyue, and J.F. Shiang. Photonic mixers and image-rejection mixers for optical SCM systems. *IEEE Transactions on Microwave Theory and Techniques*, 45(8):1478–1480, August 1997. Conference Name: IEEE Transactions on Microwave Theory and Techniques.

[30] Tianwei Jiang, Song Yu, Ruihuan Wu, Dongsheng Wang, and Wanyi Gu. Photonic downconversion with tunable wideband phase shift. *Optics Letters*, 41(11):2640–2643, June 2016. Publisher: Optica Publishing Group.

[31] S.J. Strutz, P. Biernacki, L. Nichols, and K.J. Williams. Demonstration of a wide-band image rejection microwave downconverter. *IEEE Photonics Technology Letters*, 12(6):687–689, June 2000. Conference Name: IEEE Photonics Technology Letters.

[32] Zhenzhou Tang and Shilong Pan. A Reconfigurable Photonic Microwave Mixer Using a 90° Optical Hybrid. *IEEE Transactions on Microwave Theory and Techniques*, 64(9):3017–3025, September 2016. Conference Name: IEEE Transactions on Microwave Theory and Techniques.

[33] Zhenzhou Tang and Shilong Pan. Reconfigurable microwave photonic mixer with minimized path separation and large suppression of mixing spurs. *Optics Letters*, 42(1):33–36, January 2017. Publisher: Optica Publishing Group.

[34] Ziyi Meng, Jianqiang Li, Chunjing Yin, Yuting Fan, Feifei Yin, Yue Zhou, Yitang Dai, and Kun Xu. Dual-band dechirping LFMCW radar receiver with high image rejection using microwave photonic I/Q mixer. *Optics Express*, 25(18):22055–22065, September 2017. Publisher: Optica Publishing Group.

[35] Wenjuan Chen, Dan Zhu, and Shilong Pan. Multi-octave image-reject mixer with large suppression of mixing spurs based on balanced photodetectors. In *Conference on Lasers and Electro-Optics (2018), paper STu3B.3*, page STu3B.3. Optica Publishing Group, May 2018.

[36] Dan Zhu, Wenjuan Chen, and Shilong Pan. Photonics-enabled balanced Hartley architecture for broadband image-reject microwave mixing. *Optics Express*, 26(21):28022–28029, October 2018. Publisher: Optica Publishing Group.

[37] Zhan Shi, Sha Zhu, Ming Li, Ning Hua Zhu, and Wei Li. Reconfigurable microwave photonic mixer based on dual-polarization dual-parallel Mach–Zehnder modulator. *Optics Communications*, 428:131–135, December 2018.

[38] Zhaoyang Tu, Aijun Wen, Wu Zhang, Zhongguo Xiu, and Guocong Yu. All-optical image-reject frequency down-conversion based on cascaded electro-optical modulators. *Optics Communications*, 430:158–162, January 2019.

[39] Peixuan Li, Wei Pan, Xihua Zou, Bing Lu, Lianshan Yan, and Bin Luo. Image-Free Microwave Photonic Down-Conversion Approach for Fiber-Optic Antenna Remoting. *IEEE Journal of Quantum Electronics*, 53(4):1–8, August 2017. Conference Name: IEEE Journal of Quantum Electronics.

[40] Xi Kong, Yuan Yu, Haitao Tang, and Xinliang Zhang. Microwave Photonic Image-Reject Mixer Based on a Tunable Microwave Photonic Filter With High Rejection. *IEEE Photonics Journal*, 10(6):1–11, December 2018. Conference Name: IEEE Photonics Journal.

[41] Yongsheng Gao, Aijun Wen, Wei Jiang, Yangyu Fan, and You He. All-optical and broadband microwave fundamental/sub-harmonic I/Q down-converters. *Optics Express*, 26(6):7336–7350, March 2018. Publisher: Optica Publishing Group.

[42] Yongsheng Gao, Aijun Wen, Wei Chen, and Xiaoyan Li. All-optical, ultra-wideband microwave I/Q mixer and image-reject frequency down-converter. *Optics Letters*, 42(6):1105–1108, March 2017. Publisher: Optica Publishing Group.

[43] Tsung-Ju Lu, Michael Fanto, Hyeongrak Choi, Paul Thomas, Jeffrey Steidle, Sara Mouradian, Wei Kong, Di Zhu, Hyowon Moon, Karl Berggren, Jeehwan Kim, Mohammad Soltani, Stefan Preble, and Dirk Englund. Aluminum nitride integrated photonics platform for the ultraviolet to visible spectrum. *Optics Express*, 26(9):11147–11160, April 2018. Publisher: Optica Publishing Group.

[44] A. Soltani, A. Stolz, J. Charrier, M. Mattalah, J.-C. Gerbedoen, H. A. Barkad, V. Mortet, M. Rousseau, N. Bourzgui, A. BenMoussa, and J.-C. De Jaeger. Dispersion properties and low infrared optical losses in epitaxial AlN on sapphire substrate in the visible and infrared range. *Journal of Applied Physics*, 115(16):163515, April 2014.

[45] G. F. Iriarte, J. G. Rodríguez, and F. Calle. Synthesis of c-axis oriented AlN thin films on different substrates: A review. *Materials Research Bulletin*, 45(9):1039–1045, September 2010.

[46] A. Stolz, A. Soltani, B. Abdallah, J. Charrier, D. Deresmes, P.-Y. Jouan, M.A. Djouadi, E. Dogheche, and J.-C. De Jaeger. Optical properties of aluminum nitride thin films grown by direct-current magnetron sputtering close to epitaxy. *Thin Solid Films*, 534:442–445, May 2013.

[47] W. Bogaerts, P. De Heyn, T. Van Vaerenbergh, K. De Vos, S. Kumar Selvaraja, T. Claes, P. Dumon, P. Bienstman, D. Van Thourhout, and R. Baets. Silicon microring resonators. *Laser & Photonics Reviews*, 6(1):47–73, January 2012.

[48] S. Long, M. McAllister, and Liang Shen. The resonant cylindrical dielectric cavity antenna. *IEEE Transactions on Antennas and Propagation*, 31(3):406–412, May 1983.

[49] Rajesh K. Mongia and Prakash Bhartia. Dielectric resonator antennas—a review and general design relations for resonant frequency and bandwidth. *International Journal of Microwave and Millimeter-Wave Computer-Aided Engineering*, 4(3):230–247, July 1994.

[50] S. Keyrouz and D. Caratelli. Dielectric Resonator Antennas: Basic Concepts, Design Guidelines, and Recent Developments at Millimeter-Wave Frequencies. *International Journal of Antennas and Propagation*, 2016:1–20, 2016.

[51] Wei Fu, Mingrui Xu, Xianwen Liu, Chang-Ling Zou, Changchun Zhong, Xu Han, Mohan Shen, Yuntao Xu, Risheng Cheng, Sihao Wang, Liang Jiang, and Hong X. Tang. Cavity electro-optic circuit for microwave-to-optical conversion in the quantum ground state. *Physical Review A*, 103(5):053504, May 2021.

[52] Rick C. J. Hsu, Ali Ayazi, Bijan Houshmand, and Bahram Jalali. All-dielectric photonic-assisted radio front-end technology. *Nature Photonics*, 1(9):535–538, September 2007.

[53] Ali Ayazi, Rick C. J. Hsu, Bijan Houshmand, William H. Steier, and Bahram Jalali. All-dielectric photonic-assisted wireless receiver. *Optics Express*, 16(3):1742–1747, February 2008. Publisher: Optica Publishing Group.

[54] P. Gräupner, J. C. Pommier, A. Cachard, and J. L. Coutaz. Electro-optical effect in aluminum nitride waveguides. *Journal of Applied Physics*, 71(9):4136–4139, May 1992.

[55] Shuai Liu, Ke Xu, Qinghai Song, Zhenzhou Cheng, and Hon Tsang. Design of Mid-infrared electro-optic modulators based on aluminum nitride waveguides. *Journal of Lightwave Technology*, pages 1–1, 2016.

[56] Shiyang Zhu and Guo-Qiang Lo. Aluminum nitride electro-optic phase shifter for backend integration on silicon. *Optics Express*, 24(12):12501, June 2016.

[57] Xianwen Liu, Changzheng Sun, Bing Xiong, Lai Wang, Jian Wang, Yanjun Han, Zhibiao Hao, Hongtao Li, Yi Luo, Jianchang Yan, Tongbo Wei, Yun Zhang, and Junxi Wang. Aluminum nitride-on-sapphire platform for integrated high-Q microresonators. *Optics Express*, 25(2):587, January 2017.

[58] Alexander W. Bruch, Xianwen Liu, Xiang Guo, Joshua B. Surya, Zheng Gong, Liang Zhang, Junxi Wang, Jianchang Yan, and Hong X. Tang. 17 000%/W second-harmonic conversion efficiency in single-crystalline aluminum nitride microresonators. *Applied Physics Letters*, 113(13):131102, September 2018.

[59] Joshua B. Surya, Xiang Guo, Chang-Ling Zou, and Hong X. Tang. Control of second-harmonic generation in doubly resonant aluminum nitride microrings to address a rubidium two-photon clock transition. *Optics Letters*, 43(11):2696, June 2018.

[60] Chi Xiong, Wolfram H P Pernice, Xiankai Sun, Carsten Schuck, King Y Fong, and Hong X Tang. Aluminum nitride as a new material for chip-scale optomechanics and nonlinear optics. *New Journal of Physics*, 14(9):095014, September 2012.

[61] Xiang Guo, Chang-ling Zou, Carsten Schuck, Hojoong Jung, Risheng Cheng, and Hong X Tang. Parametric down-conversion photon-pair source on a nanophotonic chip. *Light: Science & Applications*, 6(5):e16249–e16249, November 2016.

[62] Hojoong Jung and Hong X. Tang. Aluminum nitride as nonlinear optical material for on-chip frequency comb generation and frequency conversion. *Nanophotonics*, 5(2):263–271, June 2016.

[63] Hojoong Jung, King Y. Fong, Chi Xiong, and Hong X. Tang. Electrical tuning and switching of an optical frequency comb generated in aluminum nitride microring resonators. *Optics Letters*, 39(1):84, January 2014.

[64] Zheng Gong, Alexander Bruch, Mohan Shen, Xiang Guo, Hojoong Jung, Linran Fan, Xianwen Liu, Liang Zhang, Junxi Wang, Jinmin Li, Jianchang Yan, and Hong X. Tang. High-fidelity cavity soliton generation in crystalline AlN micro-ring resonators. *Optics Letters*, 43(18):4366, September 2018.

[65] Xingyu Zhang, Amir Hosseini, Harish Subbaraman, Shiyi Wang, Qiwen Zhan, Jingdong Luo, Alex K.-Y. Jen, and Ray T. Chen. Integrated Photonic Electromagnetic Field Sensor Based on Broadband Bowtie Antenna Coupled Silicon Organic Hybrid Modulator. *Journal of Lightwave Technology*, 32(20):3774–3784, October 2014. Conference Name: Journal of Lightwave Technology.

[66] John M. Wyrwas and Ming C. Wu. Frequency-modulated microwave photonic links for high dynamic-range antenna remoting systems. In *2011 IEEE Avionics, Fiber- Optics and Photonics Technology Conference*, pages 53–54, October 2011.

[67] Giovanni Serafino, Salvatore Maresca, Claudio Porzi, Filippo Scotti, Paolo Ghelfi, and Antonella Bogoni. Microwave Photonics for Remote Sensing: From Basic Concepts to High-Level Functionalities. *Journal of Lightwave Technology*, 38(19):5339–5355, October 2020. Conference Name: Journal of Lightwave Technology.

[68] David Marpaung, Jianping Yao, and José Capmany. Integrated microwave photonics. *Nature Photonics*, 13(2):80–90, February 2019. Number: 2 Publisher: Nature Publishing Group.

[69] Stefan Abel, Felix Eltes, J. Elliott Ortmann, Andreas Messner, Pau Castera, Tino Wagner, Darius Urbonas, Alvaro Rosa, Ana M. Gutierrez, Domenico Tulli, Ping Ma, Benedikt Baeuerle, Arne Josten, Wolfgang Heni, Daniele Caimi, Lukas Czornomaz, Alexander A. Demkov, Juerg Leuthold, Pablo Sanchis, and Jean Fompeyrine. Large Pockels effect in micro- and nanostructured barium titanate integrated on silicon. *Nature Materials*, 18(1):42–47, January 2019. Number: 1 Publisher: Nature Publishing Group.

[70] Stefan Abel, Thilo Stöferle, Chiara Marchiori, Daniele Caimi, Lukas Czornomaz, Christophe Rossel, Marta D. Rossell, Rolf Erni, Marilyne Sousa, Heinz Siegwart, Jens Hofrichter, Michael Stuckelberger, Alexei Chelnokov, Bert J. Offrein, and Jean Fompeyrine. Electro-Optical Active Barium Titanate Thin Films in Silicon Photonics Devices. In *Advanced Photonics 2013 (2013), paper IW4A.5*, page IW4A.5. Optica Publishing Group, July 2013.

[71] Mark Lee, Howard E. Katz, Christoph Erben, Douglas M. Gill, Padma Gopalan, Joerg D. Heber, and David J. McGee. Broadband Modulation of Light by Using an Electro-Optic Polymer. *Science*, 298(5597):1401–1403, November 2002. Publisher: American Association for the Advancement of Science.

[72] Kun-Liang Chen, Xing Jiang, and Ji-Heng Wang. Design of Dielectric Resonant Antenna (DRA) Array for 77GHz Automotive Radar Application. In *2022 International Conference on Microwave and Millimeter Wave Technology (ICMMT)*, pages 1–3, August 2022.

[73] Atabak Rashidian, David M. Klymyshyn, Mohammadreza Tayfeh Aligodarz, Martin Boerner, and Jürgen Mohr. Photoresist-Based Polymer Resonator Antennas: Lithography Fabrication, Strip-Fed Excitation, and Multimode Operation. *IEEE Antennas and Propagation Magazine*, 53(4):16–27, August 2011. Conference Name: IEEE Antennas and Propagation Magazine.

[74] M. Tayfeh Aligodarz, A. Rashidian, D. M. Klymyshyn, M. Schulz, M. Boerner, T. Hanemann, P. Meyer, and J. Mohr. Polyester-styrene/ceramic nanocomposites for antenna applications. In *2013 IEEE Antennas and Propagation Society International Symposium (APSURSI)*, pages 1906–1907, July 2013. ISSN: 1947-1491.

[75] Zhen-Xing Xia, Kwok Wa Leung, and Kai Lu. 3-D-Printed Wideband Multi-Ring Dielectric Resonator Antenna. *IEEE Antennas and Wireless Propagation Letters*, 18(10):2110–2114, October 2019. Conference Name: IEEE Antennas and Wireless Propagation Letters.